

Article

LFNMR-Informed Multi-Phase Moisture Modelling of Wood Biodegradation by *Coniophora puteana*

Royson Donate Dsouza ^{1,*}, Tiina Belt ² and Stefania Fortino ¹

¹ VTT Technical Research Centre of Finland Ltd., VTT, P.O. Box 1000, 02044 Espoo, Finland; stefania.fortino@vtt.fi

² Production Systems Unit, Natural Resources Institute Finland, Viikinkaari 9, 00790 Helsinki, Finland; tiina.belt@aalto.fi

* Correspondence: royson.dsouza@vtt.fi

Abstract

Fungal decay fundamentally alters moisture transport in wood through complex bio-physical coupling mechanisms that remain poorly understood. Brown-rot fungi such as *Coniophora puteana* (Schumach.: Fr.) P. Karst. degrade wood through chelator-mediated Fenton (CMF) chemistry, producing hydroxyl radicals that depolymerise cellulose and hemicellulose before significant mass loss. This diffusion-dependent process requires elevated moisture content and leads to structural degradation. However, existing models fail to capture the interaction between boundary-driven fungal colonization, decay-induced property changes, and multi-phase multi-Fickian moisture redistribution, particularly the separate evolution of bound- and free-water phases during decay. Here, we present a transport-response bio-hygrothermal finite element model that couples boundary-driven Monod-type fungal colonization kinetics with multi-phase moisture transport (free water, bound water, vapor) in decaying wood. Although fungal biomass evolution is simulated via a reaction–diffusion equation, decay progression is not derived from biomass–substrate interaction but prescribed independently as an experimentally informed input. The model incorporates decay-modified sorption isotherms, permeability evolution, and boundary-driven biomass influx, along with associated moisture transport, into the governing equations. The model is validated against low-field nuclear magnetic resonance (LF-NMR) measurements of *C. puteana* decay in Scots pine over 35 days. The model successfully reproduces the experimentally observed moisture evolution: a peak free-water content of 50%–70% during weeks 1–2, followed by a progressive decline, while bound water remains remarkably constant despite advancing decay. Monte Carlo uncertainty quantification demonstrates hierarchical parameter control: bound water is governed solely by thermodynamic factors, while free water responds to interacting biological and physical processes. Time-resolved correlation analysis shows a fundamental transition from colonization-dominated (weeks 1–2) to transport-dominated (weeks 3–5) moisture control, quantitatively explaining the experimentally observed shift from accumulation to depletion. This transport-response framework for analyzing moisture behavior under externally defined decay progression establishes quantitative parameter hierarchies that may inform the development of future substrate-coupled bio-hygrothermal models.



Academic Editor: Alain Cloutier

Received: 11 February 2026

Revised: 31 March 2026

Accepted: 12 April 2026

Published: 16 April 2026

Copyright: © 2026 by the authors.

Licensee MDPI, Basel, Switzerland.

This article is an open access article

distributed under the terms and

conditions of the [Creative Commons](https://creativecommons.org/licenses/by/4.0/)

[Attribution \(CC BY\)](https://creativecommons.org/licenses/by/4.0/) license.

Keywords: fungal decay; multi-Fickian; moisture transport; free water; LFNMR; finite element modeling

1. Introduction

Wood stands as a cornerstone material in construction and various industries, valued for its strength, workability, and aesthetic appeal. However, its organic composition makes it susceptible to biological agents, among which wood-decay fungi are one of the most significant threats to its long-term durability [1–3]. This biological degradation, commonly referred to as wood decay or rot, poses substantial economic challenges through the necessity for frequent repairs, replacements, and preventative treatments in buildings, infrastructure, and other wooden structures.

One of the key prerequisites for fungal wood degradation is the presence of moisture; wood-decay fungi cannot colonize dry wood, and keeping wood dry is the most effective way to prevent decay [4]. Wood is a hygroscopic material that absorbs water in two forms: bound water held within the cell wall and free water in larger pores, such as luminal spaces. Bound-water uptake causes wood to swell and influences properties such as strength and diffusivity, whereas free water appears only when the cell walls are nearly saturated. Post saturation, additional moisture resides as capillary water in pores and has comparatively little effect on wood's physical properties [5,6]. *Coniophora puteana* (Schumach.: Fr.) P. Karst., commonly known as the cellar fungus or wet rot fungus, is a widespread and notably destructive species of brown rot that frequently attacks timber in buildings, particularly in environments marked by elevated moisture levels [7]. The ability of *C. puteana* to thrive in damp conditions and to infest various locations within buildings makes it a critical species for study in the context of maintaining structural integrity.

Recent studies have shown a complex, two-way relationship between fungal activity and wood moisture content. Sufficient moisture is required for fungi to live and use their degradative agents; however, wood-decay fungi actively alter how moisture behaves within the wood they attack. Specifically, brown-rot fungi create water as a byproduct when they break down carbohydrates (a process called respiration) and can also move external water into the wood using their thread-like structures (mycelial strands) [8]. *C. puteana*, in particular, has been shown to significantly elevate the local moisture content of the wood before substantial wood weight loss [9,10].

Advances in low-field nuclear magnetic resonance (LF-NMR) and magnetic resonance imaging (MRI) have enabled monitoring of moisture changes during fungal attack. These techniques can measure water in wood across the full moisture range, from dry to completely water-saturated conditions [11]. Nuclear magnetic resonance (NMR) relaxometry can distinguish bound and free water in wood based on proton mobility, which allows one to quantify each component's response to fungal decay [7,12–14]. Muller et al. [15] used MRI to show that decay causes local areas of increased moisture. This fungus-made water creates “wet areas” where decay is just starting. These areas are visible using MRI/NMR even before you can measure any weight loss, density drop, or strength loss. These results match the observation that brown-rot decay can cause severe strength loss with very little wood weight loss (due to cell-wall polymer depolymerization) while also moving water around inside the wood [16,17]. To summarize, wood-decay fungi create conditions favorable to their spread by generating water and reducing wood substance, which in turn increases wood's ability to hold moisture.

Using LF-NMR and MRI, Hiltunen et al. [7] followed *C. puteana* decay in Scots pine and found that fungal colonization increases in free-water content inside the wood. This finding confirms that the fungus both produces water and draws in external moisture. They observed that free water was present in regions of active fungal growth (as detected by MRI signal), whereas undecayed regions remained dry, supporting the idea that the fungus elevates the local humidity and wetness of its microenvironment. Additional NMR relaxation experiments further revealed microstructural changes: degraded wood exhibited

longer T^2 relaxation times, indicative of higher-mobility water in enlarged pores or voids created by decay [7]. Beck et al. [18] similarly reported via low-field NMR that brown-rot attack alters wood–water relations, for instance by increasing the proportion of capillary (free) water at saturation. These experimental findings collectively emphasize that fungal decay is strongly linked to moisture: the amount, type, and location of water in the wood are key factors in determining how active the fungus is [4].

At the molecular scale, brown-rot decay is driven by chelator-mediated Fenton (CMF) chemistry, in which fungal chelators reduce Fe(III) to Fe(II), generating hydroxyl radicals that depolymerize cellulose and hemicellulose prior to significant mass loss [19–21]. This depolymerization leads to early loss of mechanical properties [1] and microstructural changes (increased cell-wall porosity, altered micro-capillary geometry) that affect moisture redistribution. Explicitly resolving CMF chemistry in a transport model would require spatially resolved substrate concentrations and radical-generation rates, which are currently inaccessible. The CMF mechanism is therefore not included as a model component; instead, its net macroscopic consequences—density loss, permeability increase, and altered sorption—enter the model through externally prescribed, experimentally informed inputs.

Models of wood moisture transport are generally divided into single-phase and multi-phase approaches. Single-phase models combine the equations for bound water, free water, and water vapor into one single governing equation [22]. These models can accurately estimate bound-water movement (diffusion) when the wood is below its fiber saturation point. However, they become inaccurate when the flow of liquid water becomes the dominant factor. In contrast, multi-phase (or multi-Fickian) models explicitly treat bound water, vapor, and liquid water as separate components [23–25]. In these models, the movement of bound water and vapor is described by Fick’s law (diffusion), while the flow of free water is governed by Darcy flow [26]. Multi-phase models are more complex but can capture the full range of moisture behavior in wood, particularly above the fiber saturation point, where free-water flow dominates. Recent multi-phase models have incorporated additional physics such as heat transfer, phase change, and anisotropic transport properties [24,26,27]. These models have been validated against experimental data on untreated and treated wood under various environmental conditions, demonstrating their ability to accurately predict moisture dynamics.

At the engineering scale, fungal decay has been characterized using dose–response models that relate moisture and temperature exposure to decay hazard and service life. The Meyer–Veltrup framework for above-ground applications evaluates decay risk by comparing an exposure dose, D_{Ed} , derived from daily wood temperature and moisture content, with a material resistance dose, $D_{Rd} = D_{crit} \cdot k_{wa} \cdot k_{inh}$, where D_{crit} is the critical dose for incipient decay, k_{wa} quantifies the wetting ability of the material, and k_{inh} represents inherent protective properties against decay [28]. Related dose–response research for wood in ground contact similarly expresses decay as a function of cumulative daily temperature- and moisture-induced dose components, which are empirically linked to wood mass loss [29]. These approaches demonstrate that fungal decay is governed by both intrinsic biological durability and the time-integrated moisture and thermal conditions experienced by the wood. However, although dose–response models are valuable for hazard assessment and service-life prediction, they do not explicitly address the internal redistribution of bound and free water during active fungal colonization, which is the focus of the present study.

To our knowledge, few studies have tracked mass loss and moisture content over time during fungal decay, and no prior studies have separately quantified the dynamics of bound and free water throughout the decay process. Most existing work reports endpoint gravimetry, isolated sorption experiments, or imaging snapshots. In this work, we address

this gap. Our LF-NMR measurements comprise a series of weekly endpoint observations of the bound and free moisture contents, which are used to inform the model. The measured (mass-corrected) mass-loss curve specifically defines the wood degradation input, and we use this input in the numerical model. The experimental data used in this study have been published separately by Belt et al. [30]; accordingly, the present paper focuses exclusively on the modeling framework and its validation against those published measurements.

Integrated modeling approaches that couple fungal colonization and wood moisture movement are needed but, to date, have remained difficult to develop due to their complexity. Fully detailed mechanistic models would need to capture multi-phase transport in wood (bound-water diffusion, vapor movement, capillary flow) alongside fungal processes (how colonization initiates, CMF and enzymatic breakdown, water movement at the wood surface). This would require many parameters that are hard to measure. As a result, the current literature lacks a comprehensive model that integrates these essential aspects. In this work, we aim to bridge that gap by developing a transport-response model for analyzing moisture behavior during wood decay by *C. puteana*, that integrates boundary-driven fungal colonization processes with multi-phase moisture transport in wood. This is motivated by (a) the known strong link between moisture state and decay activity, (b) the complex multi-phase moisture transport revealed by recent studies [26,27,31], and (c) our own LF-NMR observations that decay redistributes moisture with initial accumulation followed by depletion. By embedding a boundary-driven fungal colonization mechanism and decay-modulated hygroscopicity into a multi-phase moisture model, we aim to capture the dominant behavior of the moisture transport. The model represents fungal biomass as diffusing from boundaries with associated moisture influx. Fungal decay parameters are then explored via Monte Carlo sampling (propagating uncertainty from the LF-NMR-derived mass-loss inputs) to assess model sensitivity and predictive uncertainty. By capturing the core of fungus-moisture interactions while keeping the formulation manageable, this model offers new insight into how *C. puteana* causes moisture changes in wood through surface transport and internal movement, laying the groundwork for more advanced bio-hygrothermal models of wood durability and wood-based composites in the future. We hypothesize that the observed moisture evolution during brown-rot decay—initial accumulation followed by progressive depletion—can be explained by boundary-driven fungal colonization coupled with externally prescribed decay progression and the resulting permeability enhancement, without resolving the underlying degradation chemistry.

2. Experimental

The experimental data consist of gravimetric mass loss and mass loss-corrected moisture content (MC*) data, as well as bound and free MC* calculated from LF-NMR data. MC* refers to the moisture content normalized by the initial dry mass rather than the current (decaying) dry mass, which accounts for progressive wood degradation. Two nearly identical time-series decay tests were run, and data from one of these tests were used for modeling. The experimental procedure and key methods are summarized below; full details of the decay tests are provided in [30].

2.1. Decay Test and LF-NMR Method

The test samples were small Scots pine (*Pinus sylvestris*) sapwood cylinders (10 mm length, 6 mm diameter), with the cylinder axis aligned along the longitudinal (fibre) direction. They were dried at 105 °C and weighed to record their initial dry mass (average initial dry mass of 154 mg), conditioned at 85% RH, and then sterilized by autoclaving. The decay test was a time-series test with 5 harvest time points, including a time-0 point, comprising samples harvested immediately after sterilization, with $n = 10$ replicate sam-

ples per time point. The decay test was conducted in screw-cap plastic jars that contained malt extract agar inoculated with *Coniophora puteana* (BAM Ebw. 15). Wireless moisture loggers (Aqara Temperature and Humidity Sensor T1) were placed on two jars to monitor RH and temperature over the course of decay. The sterilized samples were placed in the containers over fully developed *C. puteana* mycelium growing on the nutrient agar, with plastic mesh placed between the samples and agar to prevent direct moisture absorption. The containers were incubated for 5 weeks at room temperature, with 10 samples harvested after 1, 2, 3, 4 and 5 weeks of incubation. The samples were brushed to remove surface mycelium, immediately weighed to record their decaying mass, and then tightly wrapped in plastic and stored at $-20\text{ }^{\circ}\text{C}$ until LF-NMR measurements. After LF-NMR, the samples were again dried and weighed to record their final dry mass. Mass loss (ML) and mass loss-corrected gravimetric moisture content (MC*) were calculated as follows:

$$\text{ML}(\%) = \frac{m_{\text{init}} - m_{\text{final}}}{m_{\text{init}}} \times 100\% \quad (1)$$

$$\text{MC}^*(\%) = \frac{m_{\text{decaying}} - m_{\text{final}}}{m_{\text{init}}} \times 100\% \quad (2)$$

where m_{init} is the initial dry mass, m_{final} is the final dry mass, and m_{decaying} is the decaying wet mass. Mass loss-corrected moisture content (MC*) is used because a progressive decrease in final sample mass can lead to a misleading increase in moisture content if no mass loss correction is applied.

The LF-NMR measurements were performed at $23\text{ }^{\circ}\text{C}$ on a Bruker mq20 Minispec spectrometer (Bruker, Billerica, MA, USA) with a Bruker BVT 3000 nitrogen temperature control unit. Spin-spin relaxation time (T_2) measurements were performed using a one-dimensional Carr–Purcell–Meiboom–Gill (CPMG) pulse sequence [32,33] with a 0.04 ms pulse separation, 32,000 echoes, 16 scans, and a 10 s recycle delay. The CPMG decay curves were transformed into continuous distributions of T_2 values by continuous non-negative least squares (NNLS) fitting [34,35]. For quantitative analysis of bound and free-water content, the peaks on the T_2 distributions were identified and assigned to bound water and free water based on the literature [12,36–38]. The areas of the peaks were determined, and bound-water content ($\text{MC}_{\text{bound}}^*$) and free-water content ($\text{MC}_{\text{free}}^*$) were calculated as follows:

$$\text{MC}_{\text{bound}}^*(\%) = \frac{A_{\text{bound}}}{A_{\text{total}}} \times \text{MC}^* \quad (3)$$

$$\text{MC}_{\text{free}}^*(\%) = \frac{A_{\text{free}}}{A_{\text{total}}} \times \text{MC}^* \quad (4)$$

where A_{bound} is the T_2 peak area of the bound-water peak, A_{free} is the T_2 peak area of the free-water peak(s), A_{total} total T_2 peak area, and MC^* mass loss-corrected gravimetric MC*.

2.2. Key Experimental Results

Note: This subsection summarizes the main experimental observations that directly motivate the modeling assumptions and is included here to provide the necessary context for understanding the proposed modeling approach in Section 3.

The key experimental results are summarized in Figure 1. Average mass loss increased with decay test time. Mass loss remained below 1% during the first two weeks, after which it increased to 8% at week 3, to 17% at week 4, and finally to 46% at week 5. Average gravimetric MC* on the other hand decreased over time from an initial value of 103% (week 1) to a final value of 55% (week 5). Bound MC* calculated from the LF-NMR data showed little change as a function of time, while free MC* decreased over time at the same rate as gravimetric MC*. When plotted as a function of mass loss, both gravimetric MC*

and free MC* decreased gradually, while bound MC* showed no changes as a function of mass. The other decay test revealed similar moisture trends as a function of mass loss [30].

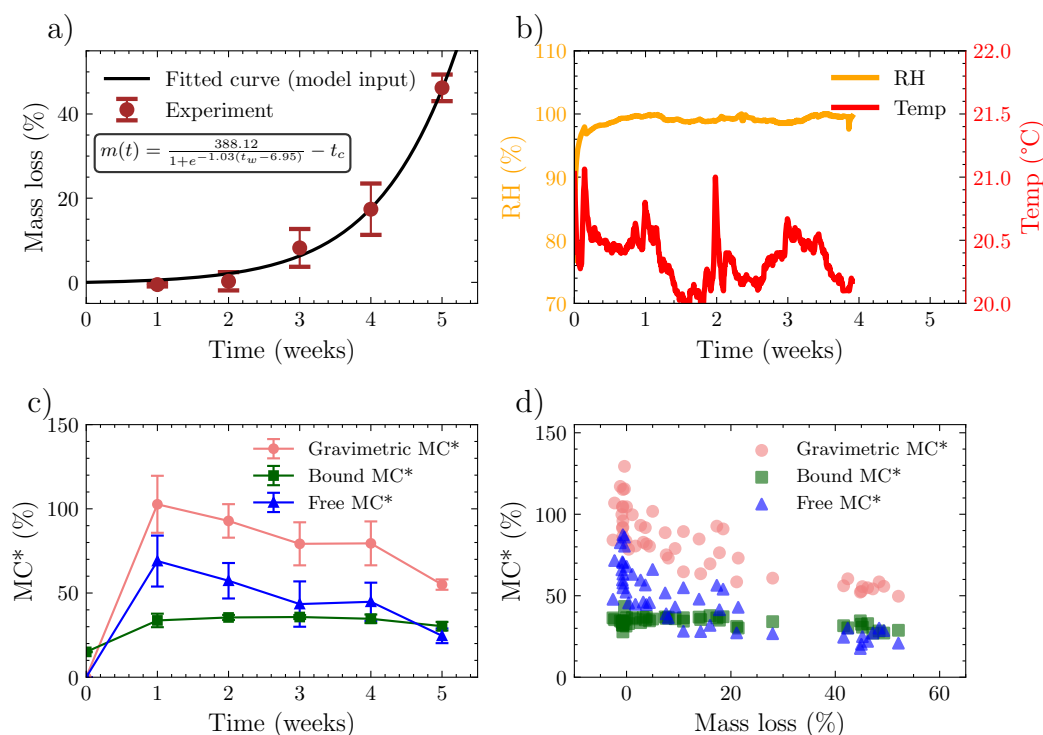


Figure 1. Experimental results from the time-series decay test with *C. puteana*: (a) mass-loss progression over time with the fitted logistic function $m(t_w) = 388.12 / (1 + e^{-1.03(t_w - 6.95)}) - t_c$, where t_w is time in weeks and t_c is the critical time, used as input to the model (Equation (32)), (b) relative humidity and temperature conditions during the experiment, (c) moisture content components (gravimetric MC*, bound MC*, and free MC*) as a function of time, and (d) moisture content components as a function of mass loss. Error bars represent standard deviation.

The time-series decay test revealed surprising moisture trends in wood degraded by *C. puteana*. It is generally thought that gravimetric MC* increases during fungal decay because fungi transport water into wood [9,10] and because fungal carbohydrate hydrolysis generates water [8]. Fungal moisture transport clearly occurred during the test, as evidenced by the very high maximum gravimetric MC*. However, gravimetric MC* increased only in very early decay, before measurable mass loss, and then decreased with time and with increasing mass loss. The decrease contradicts generally held assumptions about moisture behavior during decay and suggests that water either evaporates, is consumed, or is transported out of the wood during the decay process.

The bound-water content also yielded surprising results. Brown rot fungi utilize a diffusible mechanism to remove carbohydrates from the cell wall [19,20], increasing cell wall pore size and generating new cell wall space [8]. Increased porosity is expected to result in higher bound-water content. However, the LF-NMR data showed that bound MC* remained constant throughout the experiment, indicating no increase in absolute water content. Bound-water content increased on a decayed-mass basis (uncorrected bound MC) but less than expected [30]. Additional LF-NMR measurements performed on the samples after water saturation showed similar trends, demonstrating that there was no increase in the absolute water-accessible volume [30]. It is possible that *C. puteana* degraded the samples by an atypical, non-diffusible degradation mechanism that did not result in the creation of additional water-accessible cell wall volume or in the collapse of the new volume after formation due to shrinkage. The LF-NMR data indicates that both factors may play a

role [30]. Degradation patterns involving cell wall erosion [39] and cavity formation [40] have been found in wood degraded by *C. puteana*, and shrinkage is commonly observed in brown rot decayed wood, particularly after drying.

3. Proposed Modeling Approach

As seen in Section 2, wood decay by *C. puteana* involves complex interactions between fungal growth, moisture transport, and wood degradation that must be captured in a comprehensive mathematical framework. Figure 2 illustrates the key stages of this process, from initial incubation to advanced decay that form the basis of our modeling approach.

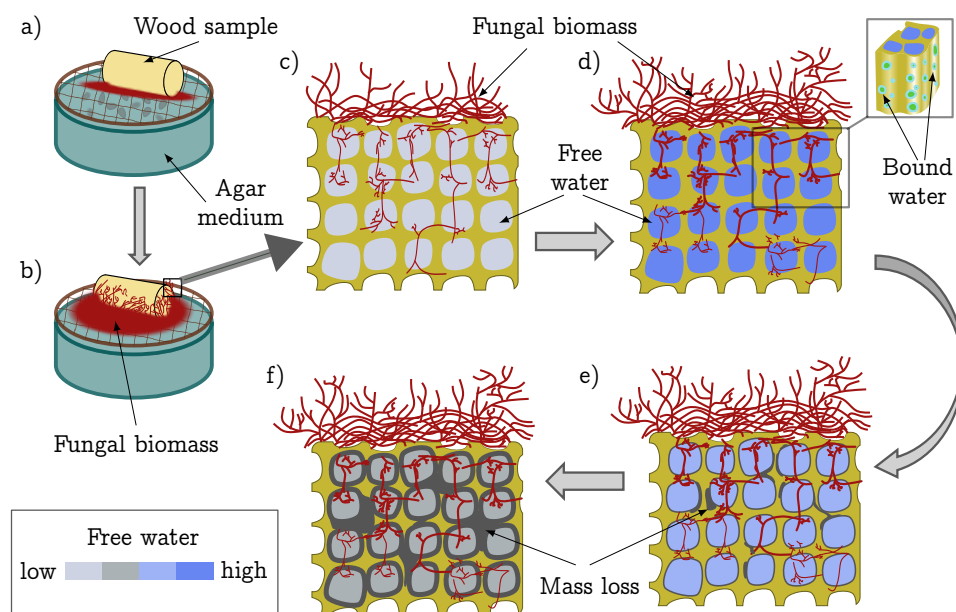


Figure 2. Conceptual representation of the decay process modeled in this study: (a) initial wood sample positioned above agar medium containing *C. puteana*, (b) fungal biomass development and initial colonization at boundaries, (c) wood sample showing internal structure, (d) progression of fungal biomass diffusion from boundaries throughout the wood matrix, (e) evolution of mass loss and moisture redistribution, and (f) development and subsequent decline of free-water content during the decay process. The figure illustrates the key processes captured by the mathematical model: boundary-driven fungal colonization, diffusion of biomass into the interior, and moisture transport from colonizing boundaries.

Figure 2 provides a conceptual map of the decay process on which our modeling framework is based. Figure 2a shows the initial configuration with sterile wood positioned above *C. puteana*-colonized agar, separated by mesh to prevent direct moisture wicking while allowing fungal contact. Figure 2b depicts the establishment phase where fungal hyphae from the agar surface begin colonizing the wood exterior, creating a biomass reservoir that drives subsequent interior invasion. Figure 2c shows the wood's internal structure that provides pathways for hyphal penetration. As shown in Figure 2d, the fungal biomass spreads through this pore network via diffusive transport from the boundaries. The colonizing boundaries serve as sources of both biomass and moisture, driving the observed moisture redistribution into the wood interior via diffusion and capillary transport. This boundary-driven moisture influx creates localized zones of elevated free-water content. Figure 2e illustrates the critical interplay between fungal activity and moisture: the evolution of mass loss and moisture decrease. Finally, Figure 2f captures the temporal evolution we seek to model—initial accumulation of free water during active boundary colonization and inward diffusive transport, followed by a decline as environmental constraints and reduced boundary fluxes dominate. This conceptual sequence, informed by our LF-NMR

observations and literature reports of brown-rot behavior, provides the physical basis for the mathematical formulation that follows.

We propose a simplified modeling approach in which the full complexity of enzymatic degradation and substrate consumption is omitted. We use the experimentally measured mass-loss curve as input to model wood property evolution. This choice allows to focus modeling efforts on the moisture-fungal interactions. Throughout this work, we distinguish between moisture content (MC), defined as the ratio of water mass to dry-wood mass, and mass loss-corrected moisture content (MC*), which accounts for changes in dry mass during decay. MC* (as described in Section 2) is used to compare model predictions with experimental measurements. The central challenge lies in representing fungal colonization and its effect on moisture. Although biomass evolution is not measured, it constitutes the critical link between wood degradation and moisture transport from the boundaries. We model fungal biomass as a continuous field that diffuses from the boundaries through the wood, approximating the penetration of hyphal networks through the pore structure. The wood samples were sterile internally, with all fungal colonization originating from the external agar surface. Surface colonization from the inoculated agar provides the boundary condition for biomass influx following modified Monod kinetics that account for temporal substrate accessibility. Once hyphae penetrate the interior via boundary-driven influx and diffusive transport, they can proliferate locally via logistic growth subject to environmental and substrate limitations. Thus the model combines boundary-driven colonization (initial biomass entry) with subsequent interior proliferation (local growth after establishment).

Moisture transport from boundaries provides the physical link between fungal colonization and moisture accumulation. As fungal mycelium colonizes from the agar surface, it transports moisture into the wood through the boundary-wood interface. The observed increase in moisture is driven by boundary influx, followed by diffusion and capillary transport into the interior. Our model treats all moisture influx as entering through the boundary conditions associated with the colonizing biomass flux. The moisture influx rate depends on boundary biomass concentration and colonization activity, explaining why free-water peaks during early active boundary colonization (weeks 1–2) and declines as boundary activity wanes and transport-dominated redistribution takes over (weeks 3–5).

The multi-phase moisture framework follows established multi-Fickian approaches but incorporates decay-induced modifications. We distinguish bound water in cell walls, free water in voids and lumens, and water vapor in air spaces—phases that align with our LF-NMR measurements. Each phase follows distinct transport mechanisms: bound water moves by solid diffusion, free water by Darcy flow, and vapor by gas diffusion. As fungal degradation progresses, the wood's pore structure evolves, significantly affecting hydraulic permeability. We model this structural evolution using a density-dependent permeability formulation, in which decreasing dry density due to mass loss leads to an exponentially increasing permeability, accelerating free-water drainage in later decay stages. The unexpected finding that bound-water MC* remains constant despite decay suggests two possibilities: either *C. puteana* uses an unusual breakdown mechanism that does not create new spaces (voids) in the cell wall, or any new spaces collapse immediately upon formation. We account for this observation using a decay-modulated sorption isotherm. This special equation maintains relatively stable bound-water levels throughout the decay, while still allowing the free-water content to vary substantially.

Parameter uncertainty presents a fundamental challenge in biological systems. Growth rates, biomass densities, and diffusion coefficients vary naturally and cannot be determined precisely from available data. We address this by performing Monte Carlo simulations, sampling parameters from physically plausible distributions to generate predictions. This

probabilistic approach provides prediction intervals rather than single deterministic outputs, allowing direct comparison with the natural scatter in experimental results.

4. Mathematical Model

The existing mathematical models for the multi-Fickian approach consist of four governing equations, each solving for the unknown degree of freedom for bound-water concentration (c_b), free-water concentration (c_w), water-vapor concentration (c_v), and temperature (T) [26,27]. To incorporate the effects of fungal degradation into this multi-Fickian framework, within the limits of the obtained LF-NMR results, we introduce a new fifth governing equation for biomass conservation and couple it to the governing equations for free-water conservation. Figure 3 provides a schematic overview of the coupled model structure, illustrating how fungal colonization from boundaries drives both biomass diffusion into the interior and moisture transport through the wood matrix.

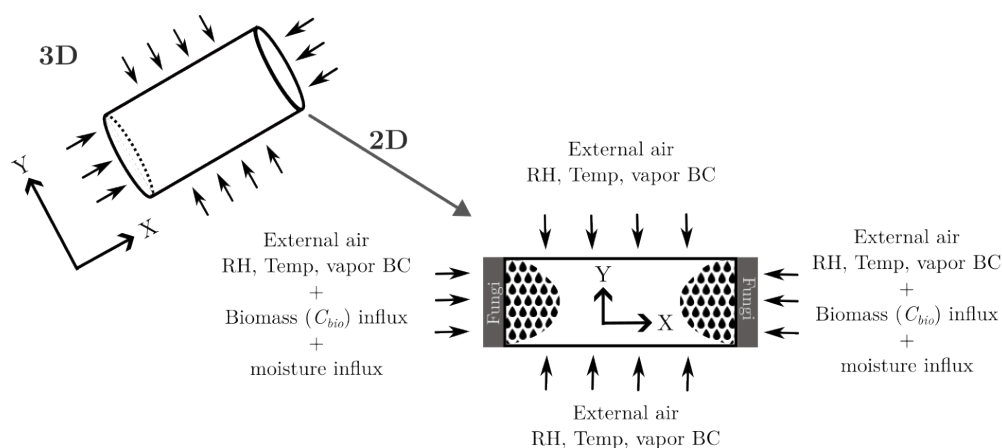


Figure 3. Conceptual representation of the mathematical model coupling fungal biomass diffusion and growth with multi-phase moisture transport in decaying wood. The model captures boundary-driven fungal colonization, diffusion of biomass into the interior, and moisture transport from colonizing boundaries.

The model comprises five coupled scalar fields: c_w (kg/m^3), c_b (kg/m^3), c_v (kg/m^3), fungal biomass concentration c_{bio} (kg/m^3), and T (K). They are defined over a 3D domain $\Omega \subset \mathbb{R}^3$ with boundary $\partial\Omega$. The equations are partial differential equations (PDEs) with diffusive transport, inter-phase transfers, and source/sink terms, all in SI units (time in seconds). The model simulates moisture redistribution and fungal colonization over the time interval $t \in (0, T^s)$. The unknown fields are c_w , c_b , c_v , c_{bio} , and T . Using these variables, we first derive the fungal biomass equation in detail, then describe how fungal activity is coupled into the moisture and energy transport equations. Finally, we summarize the full system of PDEs and present its finite-element weak-form formulations.

4.1. Fungal Biomass Conservation Equation

When a sterile wood specimen is placed in contact with an established mycelial mat of *C. puteana* growing on an agar substrate, colonization initiates at the boundaries and progresses inward. The pre-existing fungal mycelium at the wood–agar interface serves as a continuous biomass reservoir, thereby defining the boundary conditions for subsequent invasion into the wood interior. This initial colonization at the boundary demonstrates a characteristic lag phase as hyphae transition from the agar to the wood substrate, followed by exponential establishment as the mycelial network expands across the wood surface. After sufficient biomass accumulates at the boundary, hyphal tips penetrate the wood

interior primarily via the existing pore network. At the continuum scale, this invasion process can be modeled as effective diffusive transport.

The initial increase in free-water content is attributed to boundary-driven moisture influx from the colonizing mycelium. Fungal growth within wood is modeled as a continuum field for biomass, denoted as $c_{\text{bio}}(x, t)$. This continuum approach assumes that the mycelium is sufficiently dense or homogenized over a representative volume, allowing c_{bio} to be treated as a continuous variable.

For each mobile phase i , a general balance equation is formulated as follows:

$$\frac{\partial c_i}{\partial t} + \nabla \cdot \mathbf{J}_i = \dot{S}_i \quad (5)$$

Here, c_i denotes the local concentration, \mathbf{J}_i represents the flux, and \dot{S}_i is the net volumetric source or sink for that phase. A separate balance equation is established for fungal biomass c_{bio} , as well as for each moisture phase and energy. When fungal biomass is modeled as a continuous field representing mycelial density (kg/m^3) on the wood substrate, its transport and growth are governed by a reaction–diffusion mass balance:

$$\frac{\partial c_{\text{bio}}}{\partial t} + \nabla \cdot \mathbf{J}_{\text{bio}} = S_{\text{growth}} - S_{\text{mort}} \quad (6)$$

In this context, \mathbf{J}_{bio} denotes the hyphal biomass flux ($\text{kg}/(\text{m}^2 \cdot \text{s})$), S_{growth} is the local fungal growth rate (biomass production rate), and S_{mort} represents fungal mortality or decay. Equation (6) is derived from the continuum continuity equation applied to the fungal phase.

The diffusive flux \mathbf{J}_{bio} , which transports biomass from regions of high concentration (such as colonized areas near the surface) to uncolonized interior wood, is described by Fick's law. This law serves as a continuum approximation of hyphal network spread [41] and is expressed as

$$\mathbf{J}_{\text{bio}} = -D_{\text{bio}} \nabla c_{\text{bio}} \quad (7)$$

D_{bio} [m^2/s] denotes the effective mycelial diffusivity, which physically represents hyphal front growth or mycelial transport through the wood structure. Comparable reaction–diffusion models have been applied to fungal mycelium spread in soils and agar [42]. An initial value of $D_{\text{bio}} \approx 10^{-8} \text{ m}^2/\text{s}$ is adopted based on previous studies that calculated the effective diffusion coefficient for wood colonized by shiitake fungi [43]. This parameter is further varied in Monte Carlo analysis. The divergence term $\nabla \cdot \mathbf{J}_{\text{bio}} = \nabla \cdot (-D_{\text{bio}} \nabla c_{\text{bio}})$ in Equation (7) describes the spatial redistribution of biomass concentration.

4.2. Boundary Influx from Surface

A pre-established mycelial mat at the wood–agar interface serves as a continuous biomass reservoir. The transport of biomass from this external reservoir into the sterile wood interior is represented using a Robin-type boundary condition, which is analogous to convective mass transfer:

$$-\underbrace{D_{\text{bio}} \nabla c_{\text{bio}}}_{\mathbf{J}_{\text{bio}}} \cdot \mathbf{n} = \Phi_{\text{surf}} (c_{\text{biosat}} - c_{\text{bio}}) \quad (8)$$

Here, \mathbf{n} denotes the outward normal, c_{biosat} represents the saturation biomass density at the interface, and Φ_{surf} ($\text{kg}/\text{m}^2/\text{s}$) is the surface colonization rate that determines the rate at which external mycelium colonizes the wood interior. The flux is proportional to the difference between the external biomass supply and the current surface biomass, which

prevents unphysical accumulation. The parameter Φ_{surf} is derived based on Monod-type growth kinetics and mass-loss factors.

4.2.1. Monod Type Growth Kinetics

After a fungus colonizes a region of wood, its biomass increases by consuming the wood's nutrients, primarily cellulose and hemicellulose bound by lignin, and converting them into fungal cells. The local growth rate S_{growth} is modeled using a Monod kinetics formulation that incorporates environmental limitations. Originating in microbial kinetics, Monod growth describes the initial acceleration of fungal expansion, followed by a plateau as biological limitations such as nutrient availability, space, and internal regulation arise. This approach ensures that fungal uptake begins gradually, increases steadily, and then stabilizes, rather than continuing to accelerate indefinitely. In its general form, the Monod equation is [44]

$$\mu_{\text{classical}} = \mu(S) = \mu_{\text{max}} \frac{S}{K_s + S} \quad (9)$$

This is illustrated in Figure 4.

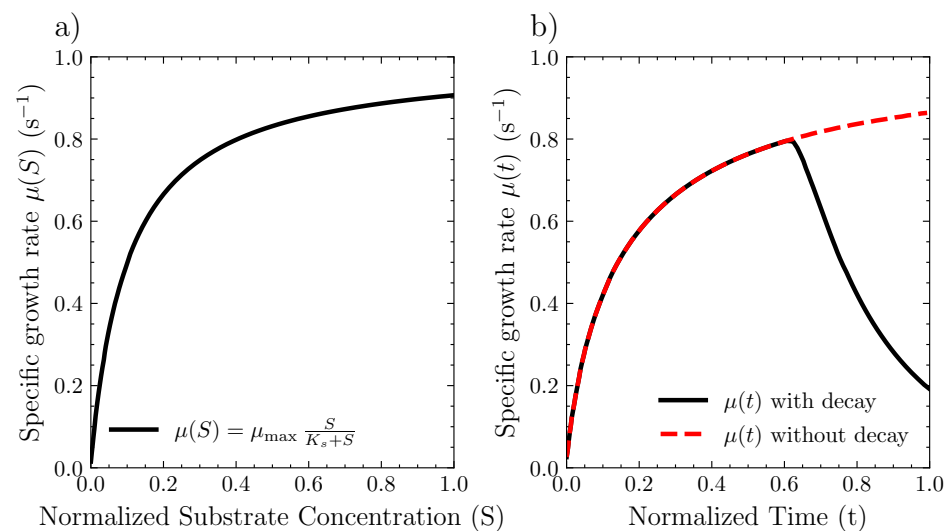


Figure 4. Monod growth kinetics: (a) classical formulation showing boundary colonization rate $\mu(S)$ as a function of normalized substrate concentration S ; (b) time-based formulation showing boundary colonization rate $\mu(t)$ as a function of normalized time t , with and without decay.

Here, $\mu_{\text{classical}}$ denotes the boundary colonization rate ($1/s$), μ_{max} is the maximum boundary colonization rate, and S represents the concentration of the limiting substrate with half-saturation constant K_s . This empirical form, originally developed for bacterial cultures and widely used [45], expresses that the boundary colonization rate increases with substrate availability but approaches μ_{max} as the substrate becomes abundant. In the context of wood decay, explicit modeling of substrate concentration is challenging due to the heterogeneous lignocellulosic composition. Therefore, substrate availability is assumed to correlate with time, reflecting initial abundance and subsequent depletion, which leads to a time-based Monod formulation:

$$\mu(t) = \mu_{\text{max}} \frac{t}{K_s + t} \quad (10)$$

In this time-based Monod model, $\mu(t)$ is now in seconds, representing the time at which the boundary colonization rate reaches half of its maximum value. This simplification avoids the need for an additional differential equation for substrate. Time is used as a surrogate for substrate concentration because spatially resolved substrate data are

unavailable during wood decay. The observed temporal progression in colonization activity supports this practical simplification.

With this the surface flux can be written as

$$\Phi_{\text{surf}}(t) = \mu(t) \cdot L_p \quad (11)$$

Hence Equation (8) can be written as

$$\mathbf{J}_{\text{bio}} \cdot \mathbf{n} = -\mu(t) L_p (c_{\text{biosat}} - c_{\text{bio}}) \quad \text{on } \partial\Omega \quad (12)$$

wherein, $\mu(t)$ is the time-accelerated Monod function from Equation (10), L_p [m] is a characteristic length scale for dimensional consistency which represents the biomass penetration depth vector varying in L , R and T directions. This boundary condition has clear physical meaning. In terms of mass balance, the boundary flux provides the sole source of biomass entering the sterile wood domain. As surface biomass density approaches c_{biosat} , further influx is suppressed, preventing unphysical accumulation. The flux increases gradually from zero, reflecting the biological reality.

4.2.2. Mechanism of Fungal Water Influx

The colonizing mycelium transports moisture from the agar substrate into the wood via hyphal channels located at the wood–agar interface. At this boundary, the water influx rate is directly proportional to the fungal activity S_{fungi} and the biomass concentration c_{bio} :

$$\text{Water influx rate} = S_{\text{fungi}} \cdot c_{\text{bio}} \quad (13)$$

Here, S_{fungi} [m/s] denotes the specific fungal water transport rate, which represents the combined effects of metabolic activity and water transport capacity. This boundary condition is applied exclusively at $\partial\Omega$ and not as an internal source term, indicating that all water influx originates at the wood–agar interface.

The metabolic activity rate incorporates three biological factors: a time-dependent Monod-type component to represent the development of substrate accessibility [46]; an environmental-decline term, adapted from Freschet et al. [47], to model the exponential reduction in activity after a critical time t_c ; and a substrate-depletion scaling that accounts for reduced activity as wood mass is consumed. The instantaneous metabolic activity rate is therefore expressed as

$$S_{\text{fungi}} = \underbrace{\left(\frac{\mu_{\text{max}} t}{K_s + t} \right)}_{\text{Monod growth}} \times \underbrace{\exp(-k_{\text{decay}}(t - t_c))}_{\text{Environmental decline}} \times \underbrace{(1 - \text{ML})}_{\text{Substrate depletion}} \quad (14)$$

By substituting Equation (14) into Equation (13), the boundary water influx rate is given by

$$\text{Water influx rate} = \frac{\mu_{\text{max}} t}{K_s + t} \cdot \exp(-k_{\text{decay}}(t - t_c)) \cdot (1 - \text{ML}) \cdot c_{\text{bio}} \quad (15)$$

The conservation equation for fungal biomass is as follows:

$$\frac{\partial c_{\text{bio}}}{\partial t} = \nabla \cdot (D_{\text{bio}} \nabla c_{\text{bio}}) + S_{\text{fungi}}(t) c_{\text{bio}} \left(1 - \frac{c_{\text{bio}}}{c_{\text{biosat}}} \right) - k_{\text{mort}} c_{\text{bio}} \quad \text{in } \Omega \quad (16)$$

This equation incorporates three mechanisms: (1) diffusive spatial redistribution via D_{bio} , which represents hyphal network expansion; (2) local logistic growth with rate $S_{\text{fungi}}(t)$ and carrying capacity c_{biosat} , describing biomass proliferation after hyphal pene-

tration into the interior; and (3) decay or mortality at rate k_{mort} . The wood samples were initially sterile, so biomass enters through the boundary condition (Equation (12)) and subsequently increases internally through the logistic growth term. This framework distinguishes between initial boundary-driven colonization and subsequent interior proliferation governed by diffusion and local growth.

4.3. Coupling of Free Water and Boundary-Driven Moisture Transport

Moisture enters the system exclusively via boundary-driven influx at $\partial\Omega$, where active colonization occurs, as quantified by Equation (13). Subsequently, water diffuses into the interior through capillary transport and vapor diffusion. The equations governing Darcy transport and coupling terms are based on established multi-Fickian models from previous work [26,27,31]. The conservation of free water in the bulk is expressed as follows:

$$\frac{\partial c_w}{\partial t} = -\nabla \cdot \left(D_w \nabla (P_g - P_c) \right) - \dot{c}_{wb} - \dot{c}_{wv} \quad \text{in } \Omega \quad (17)$$

It is important to note the absence of an internal source term S_w in Equation (17). Instead, moisture enters the system through the boundary condition:

$$\mathbf{J}_w \cdot \mathbf{n} = -k_{cw} c_w - S_{\text{fungi}} \cdot c_{\text{bio}} \quad \text{on } \partial\Omega \quad (18)$$

Here, the second term represents water influx associated with boundary colonization, which combines fungal translocation of environmental water and potential localized water release from biochemical processes at the colonization front. This formulation reflects that moisture increase is a boundary-driven phenomenon: water enters at the wood–agar interface ($\partial\Omega$) and diffuses inward through the sterile interior, rather than being generated uniformly throughout the wood volume (Ω).

Free-water flow is described by Darcy’s law, which is driven by the gradient of the difference between gaseous pressure P_g and capillary pressure P_c , as follows:

$$\mathbf{J}_w = -\rho_{\text{H}_2\text{O}} \frac{K_r K_w}{\mu_w} \nabla (P_g - P_c) \quad (19)$$

K_w denotes the absolute permeability, K_r the relative permeability, $\rho_{\text{H}_2\text{O}}$ the density of water, and μ_w the dynamic viscosity of water, as specified in [48]. The absolute permeability evolves with decay-induced structural modifications according to a density-dependent power-law relationship:

$$K_w(t) = K_w^0 \left(\frac{\rho_d^{\text{initial}}}{\rho_d(t)} \right)^\kappa \quad (20)$$

In this expression, K_w^0 is the initial absolute permeability of undecayed wood, ρ_d^{initial} is the initial dry density, $\rho_d(t)$ is the time-dependent dry density as defined in Equation (33), and κ is the permeability scaling exponent. As decay progresses and $\rho_d(t)$ decreases below ρ_d^{initial} , the permeability increases exponentially.

Table 1 summarizes the direction-dependent transport properties adopted in this work. These values were calibrated and validated for Scots pine sapwood above and below the fibre saturation point in our previous study [27].

Table 1. Anisotropic transport properties for Scots pine sapwood [27].

Property	Longitudinal (L)	Radial (R)	Tangential (T)
Liquid permeability, K_w^0 (m ²)	1×10^{-12}	2×10^{-12}	1×10^{-12}
Relative permeability, K_r (-)	S_w^{38}	S_w^3	S_w^3
Vapor resistance factor, ζ (-)	0.9	0.1	0.2
Steady-state diffusion coefficient, D_{ss} (m ² s ⁻¹)	2.5×10^{-6}	7×10^{-6}	7×10^{-6}

4.4. Bound-Water Concentration

The conservation of bound-water concentration is described by the following equation, as established in previous studies [26,27,49]:

$$\frac{\partial c_b}{\partial t} = -\nabla \cdot \mathbf{J}_b + \dot{c}_{bv} + \dot{c}_{wb} \quad \text{in } \Omega \quad (21)$$

with

$$\mathbf{J}_b \cdot \mathbf{n} = 0 \quad \text{on } \partial\Omega \quad (22)$$

The bound-water flux, J_b , is defined in Equation (21). The formulation for the bound-water diffusion tensor (\mathbf{D}_b) is provided in [49].

$$\mathbf{J}_b = - \underbrace{D_0 \exp\left(\frac{-E_b}{RT}\right)}_{D_b} \nabla c_b - D_{bT} \nabla T \quad (23)$$

The equilibrium bound-water fraction in decaying wood is represented by a decay-modulated sorption isotherm of the following form:

$$X_b^{\text{eq}}(\phi) = \left[\frac{\phi}{f_1 + f_2\phi + f_3\phi^2} \right] \cdot \psi_b \quad (24)$$

Here, the base isotherm coefficients are determined by fitting to the dynamic-vapor-sorption measurements of Dsouza et al. [27], which are valid only within the hygroscopic range. The fitted coefficients for Scots pine sapwood are: $f_{1a} = 2.099$, $f_{2a} = 13.021$, $f_{3a} = -11.883$ (adsorption) and $f_{1d} = 1.923$, $f_{2d} = 8.555$, $f_{3d} = -7.242$ (desorption). However, in experiments at relative humidities of 98% and above, this base isotherm consistently underestimates the equilibrium moisture content (MC*). To address this limitation, a tuning factor is introduced.

$$\psi_b = \left(\frac{\rho_d}{\rho_d^{\text{ini}}} \right)^\alpha \quad (25)$$

In this context, the dimensionless exponent α determines the influence of density loss on bound-water MC*. As decay advances and ρ_d decreases below ρ_d^{ini} , the density ratio becomes less than one. The value of α governs the rate of reduction: $\alpha > 1$ amplifies the effect of density loss, whereas $\alpha < 1$ moderates it.

The equilibrium bound-water concentration is therefore given by

$$c_b^{\text{eq}} = X_b^{\text{eq}}(\phi) \cdot \rho_d(t) \quad (26)$$

4.5. Water-Vapor Concentration

The conservation of water-vapor concentration is expressed as follows:

$$\frac{\partial}{\partial t} (c_v f_{\text{lum, gas}}) = -\nabla \cdot (\mathbf{J}_v f_{\text{lum, gas}}) - \dot{c}_{bv} + \dot{c}_{wv} \quad \text{in } \Omega \quad (27)$$

subject to the boundary condition

$$c_v = \text{RH} \cdot c_{v,\text{sat}} \quad \text{on } \partial\Omega \quad (28)$$

The water-vapor flux, \mathbf{J}_v , is defined as $\mathbf{J}_v = -\mathbf{D}_v \cdot \nabla c_v$ [49]. The diffusion tensor for water vapor (\mathbf{D}_v) is detailed in [25] and presented in Equation (29):

$$\mathbf{J}_v = - \underbrace{\zeta \left(2.31 \times 10^{-5} \frac{p_{\text{atm}}}{p_{\text{atm}} + p_{v,\text{air}}} \left(\frac{T}{273} \right)^{1.81} \right)}_{D_v} \nabla c_v \quad (29)$$

The saturated water-vapor concentration, $c_{v,\text{sat}}$, is calculated using the equation provided by Hailwood and Horrobin [50]:

$$c_{v,\text{sat}} = \frac{M_{\text{H}_2\text{O}}}{R T} 2.2064 \cdot 10^7 \exp \left\{ \frac{647.14}{T} \left(-7.85823 \cdot \tau + 1.83991 \cdot \tau^{1.5} - 11.7811 \cdot \tau^3 + 22.6705 \cdot \tau^{3.5} - 15.9393 \cdot \tau^4 + 1.77516 \cdot \tau^{7.5} \right) \right\} \quad (30)$$

4.6. Conservation of Energy

The energy conservation equation accounts for heat conduction, convective transport related to moisture phases, and latent heat effects arising from phase transformations:

$$\frac{\partial \rho h}{\partial t} = -\nabla \cdot \mathbf{f} - \nabla \cdot \mathbf{J}_b \bar{h}_b - \nabla \cdot \mathbf{J}_v h_v f_{\text{lum, gas}} - \nabla \cdot \mathbf{J}_w h_w + \dot{c}_{bv}(h_v - h_b) + \dot{c}_{wb}(h_w - h_b) + \dot{c}_{wv}(h_w - h_v) - S_T \quad (31)$$

Here, \mathbf{f} denotes the heat flux vector due to conduction and S_T represents volumetric heat sources or sinks, such as metabolic heat generation from fungal activity and possible exothermic reactions during decay.

4.7. Auxiliary Equations

Experimentally measured mass-loss progression obtained from LF-NMR serves as an input to the model. Weekly mean mass-loss values, as shown in Figure 1a, are fitted to a logistic function:

$$m(t_w) = \frac{388.12}{1 + e^{-1.03(t_w - 6.95)}} - t_c \quad (32)$$

Here, t_w is time expressed in weeks, t_c is the critical time, and $m(t_w)$ denotes the mass-loss percentage. This empirical function describes the sigmoidal progression from minimal loss (<1%) during weeks 1 to 2 to 46% by week 5. The evolving dry density is subsequently calculated from the mass loss:

$$\rho_d(t) = \rho_d^{\text{initial}} \cdot \left(1 - \frac{m(t)}{100} \right) \quad (33)$$

The initial dry density $\rho_d^{\text{initial}} = 530 \text{ kg/m}^3$ is the average oven-dry density of Scots pine sapwood, measured experimentally using X-ray micro-computed tomography [27]. This time-dependent density $\rho_d(t)$ directly influences the sorption equilibrium c_b^{eq} , permeability, and all transport parameters at each time step.

4.8. Numerical Solution

Summarizing Sections 4.1–4.7, the strong form of five governing differential equations can be written as follows:

For free water:

$$\begin{cases} \frac{\partial c_w}{\partial t} = -\nabla \cdot (D_w \nabla (P_g - P_c)) - \dot{c}_{wb} - \dot{c}_{wv} & \text{in } \Omega, \\ \mathbf{J}_w \cdot \mathbf{n} = -k_{cw} c_w - S_{\text{fungi}} \cdot c_{\text{bio}} & \text{on } \partial\Omega. \end{cases} \quad (34)$$

For bound water:

$$\begin{cases} \frac{\partial c_b}{\partial t} = -\nabla \cdot \mathbf{J}_b + \dot{c}_{bv} + \dot{c}_{wb} & \text{in } \Omega, \\ \mathbf{J}_b \cdot \mathbf{n} = 0 & \text{on } \partial\Omega. \end{cases} \quad (35)$$

For water vapor:

$$\begin{cases} \frac{\partial}{\partial t} (c_v f_{\text{lum_gas}}) = -\nabla \cdot (\mathbf{J}_v f_{\text{lum_gas}}) - \dot{c}_{bv} + \dot{c}_{wv} & \text{in } \Omega, \\ c_v = \text{RH} \cdot c_{v,\text{sat}} & \text{on } \partial\Omega. \end{cases} \quad (36)$$

For fungal biomass:

$$\begin{cases} \frac{\partial c_{\text{bio}}}{\partial t} = \nabla \cdot (D_{\text{bio}} \nabla c_{\text{bio}}) + c_{\text{bio}} S_{\text{fungi}} - k_{\text{mort}} c_{\text{bio}} & \text{in } \Omega, \\ \mathbf{J}_{\text{bio}} \cdot \mathbf{n} = -\mu(t) L_p (c_{\text{biosat}} - c_{\text{bio}}) & \text{on } \partial\Omega. \end{cases} \quad (37)$$

For energy:

$$\begin{aligned} \frac{\partial \rho h}{\partial t} = & -\nabla \cdot \mathbf{f} - \nabla \cdot (\mathbf{J}_b \bar{h}_b) - \nabla \cdot (\mathbf{J}_v h_v f_{\text{lum_gas}}) - \nabla \cdot (\mathbf{J}_w h_w) \\ & + \dot{c}_{bv} (h_v - h_b) + \dot{c}_{wb} (h_w - h_b) + \dot{c}_{wv} (h_w - h_v) - S_T \end{aligned} \quad (38)$$

Spatial discretization uses the finite element (FE) method on a tetrahedral mesh of Ω . The solution is approximated in a vector-valued Lagrange space of degree 1. Each time step has five unknowns. The system is discretized in time using the backward Euler method for stability in stiff fungal growth terms, with the adaptive time step Δt bounded by $\Delta t_{\min} = 60$ s and $\Delta t_{\max} = 600$ s. To obtain the weak forms, each time-discretized strong form is multiplied by a test function from the same space and integration over Ω is performed. Next, integration by parts to diffusion and flux terms (yielding boundary integrals for Neumann conditions) is applied. The total weak form ($F = F_{c_w} + F_{c_b} + F_{c_v} + F_{c_{\text{bio}}} + F_T = 0$) is the sum of the following five individual weak forms:

$$\begin{aligned} F_{c_w} = & \int_{\Omega} \left[\frac{c_w^{n+1} - c_w^n}{\Delta t} v_{c_w} + \mathbf{J}_w(c_w, c_b, T) \cdot \nabla v_{c_w} + \dot{c}_{wb}(t, c_b, c_{b,\text{eq}}, c_w, c_v) \cdot v_{c_w} \right. \\ & \left. + \dot{c}_{wv}(c_w, c_v, c_{v,\text{sat}}, f_{\text{lum_gas}}) \cdot v_{c_w} \right] dV - \int_{\partial\Omega} [k_{cw} c_w + S_{\text{fungi}}(t) \cdot c_{\text{bio}}] \cdot v_{c_w} dS \end{aligned} \quad (39)$$

$$F_{c_b} = \int_{\Omega} \left[\frac{c_b^{n+1} - c_b^n}{\Delta t} v_{c_b} + D_b(c_b) \cdot \nabla c_b \cdot \nabla v_{c_b} - \dot{c}_{wb}(t, c_b, c_{b,\text{eq}}, c_w, c_v) \cdot v_{c_b} - \dot{c}_{bv}(t, c_b, c_{b,\text{eq}}, c_v) \cdot v_{c_b} \right] dV \quad (40)$$

$$\begin{aligned} F_{c_v} = & \int_{\Omega} \left[\frac{c_v^{n+1} - c_v^n}{\Delta t} v_{c_v} + D_v(c_v) \cdot \nabla c_v \cdot \nabla v_{c_v} + \dot{c}_{bv}(t, c_b, c_{b,\text{eq}}, c_v) \cdot v_{c_v} - \right. \\ & \left. \dot{c}_{wv}(c_w, c_v, c_{v,\text{sat}}, f_{\text{lum_gas}}) \cdot v_{c_v} \right] dV + \int_{\partial\Omega} f_{\text{lum}}(c_b) \cdot k_{cv} \cdot (c_v - c_{v,\text{sat}} \cdot \text{RH}(t)) \cdot v_{c_v} dS \end{aligned} \quad (41)$$

$$F_{c_{bio}} = \int_{\Omega} \left[\frac{c_{bio}^{n+1} - c_{bio}^n}{\Delta t} v_{c_{bio}} + D_{bio} \cdot \nabla c_{bio} \cdot \nabla v_{c_{bio}} + k_{mort} \cdot c_{bio} \cdot v_{c_{bio}} - S_{fungi}(t) \cdot c_{bio} \cdot \left(1 - \frac{c_{bio}}{c_{biosat}}\right) \cdot v_{c_{bio}} \right] dV - \int_{\partial\Omega} \mu(t) \cdot \left(1 - \frac{c_{bio}}{c_{biosat}}\right) \cdot v_{c_{bio}} dS \tag{42}$$

$$F_T = \int_{\Omega} \left[\frac{(\rho h)^{n+1} - (\rho h)^n}{\Delta t} v_T + \mathbf{f} \cdot \nabla v_T + \mathbf{J}_b \bar{h}_b \cdot \nabla v_T + \mathbf{J}_v h_v f_{lum,gas} \cdot \nabla v_T + \mathbf{J}_w h_w \cdot \nabla v_T - \dot{c}_{bv} (h_v - h_b) v_T - \dot{c}_{wb} (h_w - h_b) v_T - \dot{c}_{wv} (h_w - h_v) v_T + S_T v_T \right] dV \tag{43}$$

With the five coupled equations (Equations (39)–(43)), the system of equations can be defined at each integration point as follows. The tangent stiffness matrix \mathbf{K}_t is a block 5×5 array of partial derivatives $\frac{\partial F^X}{\partial Y}$, where X (A, B, C, D, E) denotes the residual components for each governing equation ($F_{c_w}^A$ for free water, $F_{c_b}^B$ for bound water, $F_{c_v}^C$ for vapor, $F_{c_{bio}}^D$ for fungal biomass, and F_T^E for temperature). Y (P, Q, R, S, U) represents the nodal unknowns (c_w^P for free-water DOFs, etc.). The vector \mathbf{u}^k contains the solution increments $\Delta \mathbf{u}^k$ at Newton iteration k , and \mathbf{r} is the negative residual vector, assembled from the weak forms evaluated at the current \mathbf{u}^k . The linearized Newton system at each iteration is given by

$$\underbrace{\begin{bmatrix} \frac{\partial F_{c_w}^A}{\partial c_w^P} & \frac{\partial F_{c_w}^A}{\partial c_b^Q} & \frac{\partial F_{c_w}^A}{\partial c_v^R} & \frac{\partial F_{c_w}^A}{\partial c_{bio}^S} & \frac{\partial F_{c_w}^A}{\partial T^U} \\ \frac{\partial F_{c_b}^B}{\partial c_w^P} & \frac{\partial F_{c_b}^B}{\partial c_b^Q} & \frac{\partial F_{c_b}^B}{\partial c_v^R} & \frac{\partial F_{c_b}^B}{\partial c_{bio}^S} & \frac{\partial F_{c_b}^B}{\partial T^U} \\ \frac{\partial F_{c_v}^C}{\partial c_w^P} & \frac{\partial F_{c_v}^C}{\partial c_b^Q} & \frac{\partial F_{c_v}^C}{\partial c_v^R} & \frac{\partial F_{c_v}^C}{\partial c_{bio}^S} & \frac{\partial F_{c_v}^C}{\partial T^U} \\ \frac{\partial F_{c_{bio}}^D}{\partial c_w^P} & \frac{\partial F_{c_{bio}}^D}{\partial c_b^Q} & \frac{\partial F_{c_{bio}}^D}{\partial c_v^R} & \frac{\partial F_{c_{bio}}^D}{\partial c_{bio}^S} & \frac{\partial F_{c_{bio}}^D}{\partial T^U} \\ \frac{\partial F_T^E}{\partial c_w^P} & \frac{\partial F_T^E}{\partial c_b^Q} & \frac{\partial F_T^E}{\partial c_v^R} & \frac{\partial F_T^E}{\partial c_{bio}^S} & \frac{\partial F_T^E}{\partial T^U} \end{bmatrix}}_{\mathbf{K}_t} \cdot \underbrace{\begin{bmatrix} r^{c_w} \\ r^{c_b} \\ r^{c_v} \\ r^{c_{bio}} \\ r^T \end{bmatrix}}_{\mathbf{u}^k} = \underbrace{\begin{bmatrix} -F^A \\ -F^B \\ -F^C \\ -F^D \\ -F^E \end{bmatrix}}_{\mathbf{r}} \tag{44}$$

This equation is computed element-wise at Gauss quadrature points within each three-dimensional tetrahedral element, where local nonlinear terms and their derivatives are computed and integrated. The system is solved iteratively using Newton’s method until convergence, typically achieved when the norm of the increment $\|\mathbf{u}^k\|$ is less than 10^{-12} . The numerical implementation utilizes the open-source FEniCSx (dolfinx) platform (version 0.9.0), which provides high-level Python interfaces for complex multi-physics problems [51]. Dolfinx is employed for finite element assembly and nonlinear solving [51], basix is used for runtime finite element basis evaluation [52], and UFL (Unified Form Language) is used for symbolic weak-form specification [53]. Three-dimensional tetrahedral meshes are generated with Gmsh [54].

4.9. Monte Carlo Simulations

Monte Carlo simulations were conducted to address the inherent variability in fungal growth and wood decay processes. Unlike deterministic models that yield single-point estimates, Monte Carlo methods generate probability distributions by sampling from parameter ranges [55]. This approach captures both the mean trends and the variability that naturally arise in experimental observations.

For each simulation run, a parameter vector

$$\mathbf{p}_i = \left(\mu_{max}, K_s, c_{biosat}, t_c, \alpha, D_{bio}, k_{decay}, k_{mort}, \kappa \right) \tag{45}$$

was sampled from uniform distributions within the ranges summarized in Table 2, where $i = 1, \dots, N$ and $N = 300$ denotes the ensemble size.

Table 2. Monte Carlo varied parameters, their ranges, and units.

Parameter	Name	Range	Unit
μ_{\max}	Maximum growth rate	1.0×10^{-4} – 1.0×10^{-2}	s^{-1}
K_s	Half-saturation constant	3.02×10^5 – 3.02×10^6	s
c_{biosat}	Biomass saturation	30.0–50.0	kg/m ³
t_c	Critical time	5.44×10^5 – 9.07×10^5	s
α	Boost parameter	0.0–0.2	—
D_{bio}	Biomass diffusivity	5.0×10^{-13} – 5.0×10^{-9}	m ² /s
k_{decay}	Decay rate constant	2.48×10^{-7} – 9.09×10^{-7}	s^{-1}
k_{mort}	Mortality rate constant	1.0×10^{-6} – 1.0×10^{-5}	s^{-1}
κ	Permeability factor	10.0–20.0	—

Each parameter set was required to satisfy physical constraints, such as non-negativity of initial concentrations and a critical time t_c less than the total simulation horizon.

The governing equations introduced in Section 4 were solved for each parameter set to obtain the time series

$$\mathcal{Y}_i(t) = \left(c_w^{(i)}(t), c_b^{(i)}(t), c_v^{(i)}(t), c_{\text{bio}}^{(i)}(t), T^{(i)}(t) \right), \tag{46}$$

from which derived quantities, such as MC*s, were calculated according to the experimental definitions. To enable comparison across runs and with experiments, all outputs were interpolated to a common time grid t_j with hourly resolution.

4.9.1. Statistical Analysis of Ensemble Predictions

At each time point t_j , ensemble statistics were evaluated from the $N = 300$ realizations. For any output variable y (representing free-water concentration, bound-water concentration, water-vapor concentration, or biomass concentration), the ensemble mean and variance were calculated as

$$\mu_y(t_j) = \frac{1}{N} \sum_{i=1}^N y_i(t_j), \quad \sigma_y^2(t_j) = \frac{1}{N} \sum_{i=1}^N (y_i(t_j) - \mu_y(t_j))^2, \tag{47}$$

where $y_i(t_j)$ is the value of variable y from simulation i at time t_j . The empirical quantiles were computed to construct prediction intervals:

$$q_{0.05}(t_j) = P_{0.05}\{y_i(t_j)\}, \quad q_{0.95}(t_j) = P_{0.95}\{y_i(t_j)\}, \tag{48}$$

where $P_p\{\cdot\}$ denotes the p -th percentile operator. These provided 90% prediction intervals $[q_{0.05}(t_j), q_{0.95}(t_j)]$ for visualization of uncertainty bands around the ensemble mean.

Scalar metrics were extracted from each realization, including the peak free-water content

$$c_{w,i}^{\text{peak}} = \max_t c_w^{(i)}(t), \tag{49}$$

and the corresponding time to peak

$$t_{w,i}^{\text{peak}} = \arg \max_t c_w^{(i)}(t), \tag{50}$$

where $c_w^{(i)}(t)$ is the free-water concentration from simulation i at time t and $t_{w,i}^{\text{peak}}$ is the time at which the free-water concentration reaches its maximum value in simulation i .

4.9.2. Weekly Correlation Analysis

Parameter sensitivity analysis was conducted at weekly intervals corresponding to experimental measurement points: $t_k \in \{168, 336, 504, 672, 840\}$ hours (weeks 1 to 5). For each time point and each moisture component (free water, bound water, water vapor, biomass), the Spearman rank correlation coefficient was calculated between parameter values x_j (where j indexes the 10 parameters in Table 2) and model outputs $y_c(t_k)$ (where c indexes the moisture component):

$$\rho_{jc}(t_k) = 1 - \frac{6 \sum_{i=1}^N d_i^2}{N(N^2 - 1)}, \quad (51)$$

where d_i represents the difference in ranks between paired observations $x_{j,i}$ (parameter j value in simulation i) and $y_{c,i}(t_k)$ (component c output from simulation i at week k). The Spearman correlation was selected instead of the Pearson correlation to capture monotonic, nonlinear relationships. Statistical significance was evaluated using p-values, and correlations with $p < 0.05$ were considered meaningful.

4.9.3. Pareto Analysis for Parameter Importance

Pareto analysis was conducted for each moisture component to identify the most influential parameters. Two types of Pareto analysis were implemented:

Weekly Pareto analysis: For each week k and component c , the contribution of parameter j to output variance was estimated as

$$V_j(t_k) = \rho_{jc}^2(t_k), \quad (52)$$

where $\rho_{jc}(t_k)$ is the Spearman correlation between parameter j and component c at week k . The relative contribution was then calculated as

$$R_j(t_k) = \frac{V_j(t_k)}{\sum_{j'=1}^{10} V_{j'}(t_k)} \times 100\%, \quad (53)$$

and the cumulative contribution was computed as

$$C_j(t_k) = \sum_{j'=1}^j R_{j'}(t_k), \quad (54)$$

In this calculation, parameters are ordered by decreasing absolute correlation.

Overall parameter importance: To rank parameters across all weeks and components, the mean absolute correlation was calculated as

$$\bar{\rho}_j = \frac{1}{5 \times 4} \sum_{k=1}^5 \sum_{c=1}^4 |\rho_{j,c}(t_k)|, \quad (55)$$

Here, the summations are taken over the five weekly time points ($k = 1, 2, 3, 4, 5$ corresponding to weeks 1 to 5) and four moisture components ($c = 1, 2, 3, 4$ corresponding to free water, bound water, water vapor, and biomass).

Justification of parameter ranges: Quantifying the values of c_{biosat} for *C. puteana* is challenging due to limited direct values in the literature and the complexity of separating fungal biomass from wood. Therefore, parameter ranges from Nussbaumer et al. [56] are used. This study reports fungal biomass densities for *Ganoderma sessile*, *Pleurotus pulmonarius*, and *Trametes versicolor* on beech sawdust ranging from 1 to 10 kg/m³, with values up to 57 kg/m³ on nutrient-rich substrates such as apple pomace. Given *C. puteana*'s adapta-

tion to softwoods and the significant decay observed, a mycelial density range of 30 to 50 kg/m³ is adopted for this study. The range of values for D_{bio} is justified using typical diffusion coefficients in porous media such as wood. Fungal growth models, including Boswell et al. [57], discuss diffusion in mycelial networks, where substrate nutrients diffuse and are translocated, although specific numerical values are not provided. Studies on *Postia placenta*, a similar brown-rot fungus, report tip extension rates up to 28.8 $\mu\text{m}/\text{h}$ [58], which can inform effective diffusion coefficients. In porous media, diffusion coefficients for water range from 10^{-9} to 10^{-8} m²/s, and for fungal hyphae, values around 5.0×10^{-9} to 5.0×10^{-13} m²/s are reasonable estimates. The μ_{max} is estimated as a fitted value in the range of 1.0×10^{-2} to 1.0×10^{-4} to match the peak free-water MC* observed in LF-NMR experiments.

5. Results and Discussion

The sensitivity of the model to key parameters and their effects on moisture evolution during fungal decay was assessed by systematically varying seven critical parameters governing fungal growth (Equation (10)), moisture transport (Equations (19) and (24)), and decay kinetics. Each simulation covered the complete 35-day (839.7 h) experimental period.

5.1. Effect of the Boost Parameter (α) on Bound-Water MC*

The decay-modulated sorption isotherm includes the tuning factor α (Equation (25)), which scales the equilibrium bound-water MC* to account for near-saturation conditions during decay. Figure 5 presents the influence of varying α from 0.05 to 0.25 on bound-water MC* over time. α demonstrates the strongest control over bound-water MC*, with a correlation coefficient of 0.9995 averaged across all time points, indicating an almost direct proportionality between α and bound-water MC*.

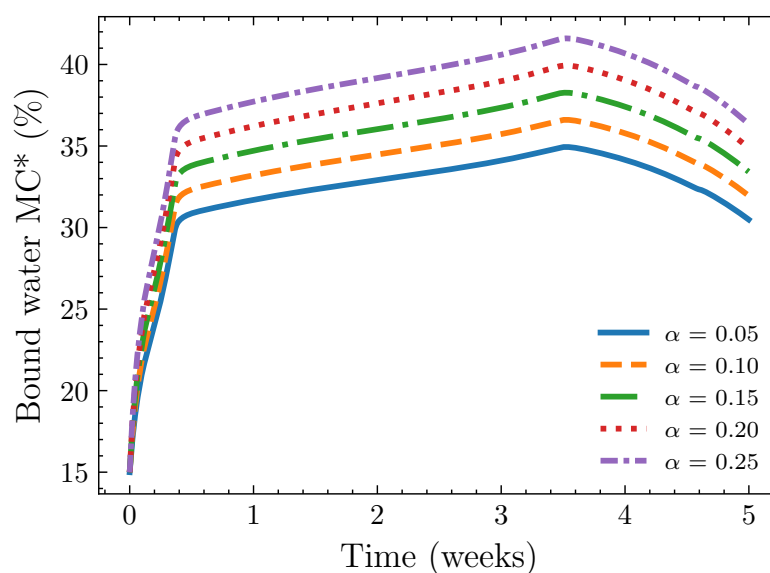


Figure 5. Effect of the boost parameter α (values from 0.05 to 0.25) on bound-water MC* evolution over the 35-day decay period.

An increase in α from 0.05 to 0.25 results in a systematic rise in bound-water MC* from approximately 30.5% to 36.4%, representing a 19% relative increase. All curves exhibit similar temporal evolution but differ in plateau magnitudes. This parameter effectively accounts for the thermodynamic correction required under high relative humidity conditions, which the base Hailwood–Horrobin sorption isotherms (Equation (24)) do not capture. The observed linear scaling with α indicates that this factor primarily influences the equilibrium MC* for

bound water, rather than the kinetics of moisture uptake. The dominance of α over bound-water MC* is a structural property of the governing equations rather than an artifact of parameter tuning. The bound-water conservation equation (Equation (21)) has zero-flux boundary conditions ($\mathbf{J}_b \cdot \mathbf{n} = 0$) and is driven toward equilibrium by phase-exchange source terms (\dot{c}_{bv} , \dot{c}_{wb}) whose rate constants are fixed material properties. At the near-saturation conditions of this experiment ($\phi \approx 1$), the equilibrium target c_b^{eq} (Equation (26)) reduces to $c_b^{\text{eq}} \approx X_b^{\text{eq}}(1) \cdot \rho_d^{\text{ini}} \cdot (1 - m/100)^{\alpha+1}$, which depends only on α and on the prescribed mass loss. The remaining seven Monte Carlo parameters (μ_{max} , K_s , c_{biosat} , D_{bio} , k_{decay} , k_{mort} , κ) enter exclusively through the biomass and free-water subsystems and cannot influence c_b^{eq} except through the negligible indirect path via relative humidity, which remains near unity throughout the decay period.

5.2. Effect of Maximum Boundary Colonization Rate (μ_{max}) and Critical Time (t_c)

μ_{max} and t_c are fundamental parameters in the time-dependent Monod-type growth kinetics (Equation (10)) that govern the rate of fungal establishment and the timing of peak colonization activity. Figure 6 illustrates their combined influence on free-water evolution.

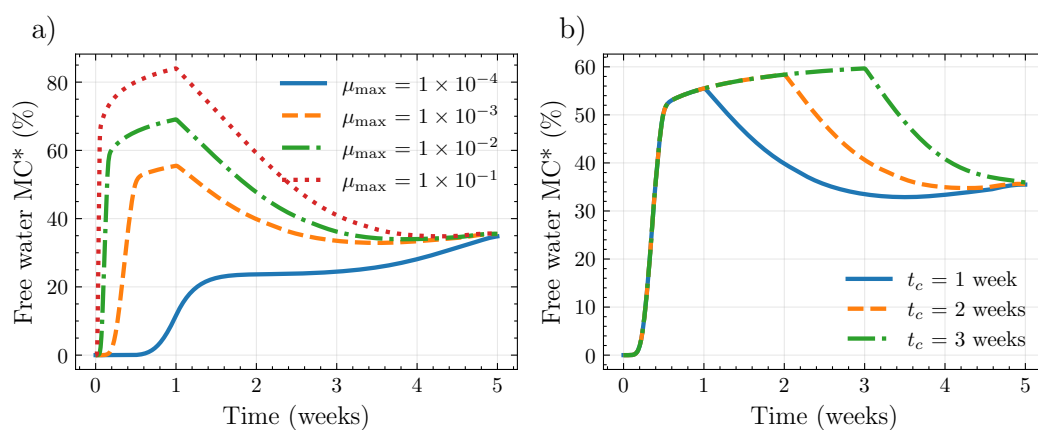


Figure 6. Effect of maximum boundary colonization rate μ_{max} and critical time t_c on free-water evolution: (a) varying μ_{max} from 10^{-4} to 10^{-1} s^{-1} ; (b) varying t_c from 1 to 3 weeks.

Figure 6a reveals that μ_{max} exerts strong control over both the magnitude and timing of free-water MC*. Lower values (10^{-4} s^{-1}) result in minimal free-water MC*, while higher values (10^{-1} s^{-1}) produce substantial peaks reaching 80%–90% free-water MC*. The timing also shifts earlier with increasing μ_{max} , indicating faster boundary colonization establishment and more rapid water influx from the agar substrate. This behavior is consistent with the experimental observations where peak free water occurs during active colonization phases.

Figure 6b shows the effect of t_c , which represents the time at which environmental conditions begin to decline (Equation (10)). Increasing t_c from 1 to 3 weeks shifts the entire free-water evolution curve later in time without substantially changing peak magnitudes. This shift reflects the delayed onset of environmental constraints that limit continued fungal activity and boundary water delivery. The nearly parallel curves indicate that t_c primarily controls timing rather than the extent of moisture influx.

5.3. Effect of Half-Saturation Constant (K_s) on Growth Kinetics and Biomass

Figure 7 illustrates the influence of K_s on both free-water evolution and fungal biomass accumulation across a two-order-of-magnitude range (10^6 to 10^8 s). Reducing K_s from 10^8 to 10^6 results in earlier and higher peaks in free-water MC* (Figure 7a). At the lowest value ($K_s = 10^6 \text{ s}$), free-water MC* reaches 31% by approximately 40 h and peaks near

50% during active colonization, closely matching experimental observations at weeks 1 and 2. In contrast, $K_s = 10^8$ s yields minimal free-water accumulation throughout the simulation, with the system remaining in a substrate-limited growth regime where $\mu(t) \ll \mu_{\max}$ (Equation (10)). Intermediate values display proportional behavior, confirming the logarithmic relationship between K_s and growth rate (see inset in Figure 7a).

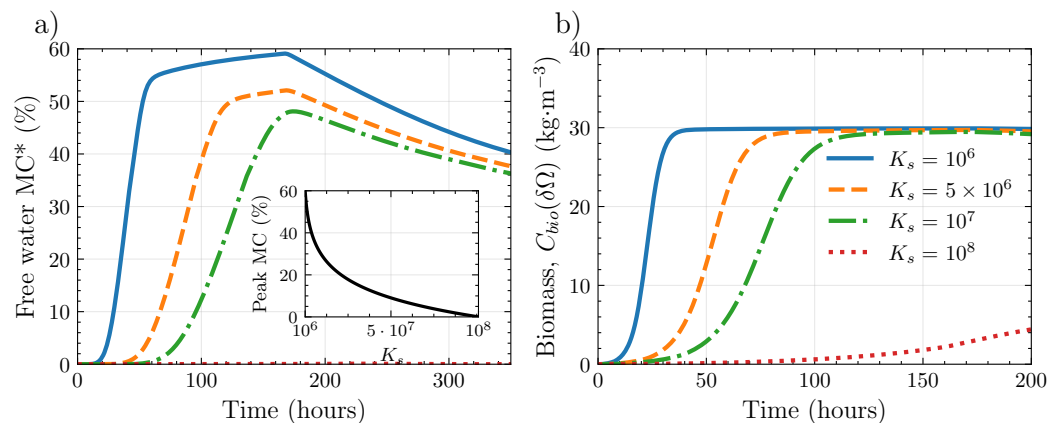


Figure 7. Effect of half-saturation constant K_s (values from 10^6 to 10^8 s) on (a) free-water MC^* and (b) fungal biomass evolution over the 35-day decay period.

Figure 7b presents the corresponding effects on fungal biomass evolution at boundaries, where the coupling between colonization kinetics and moisture transport is explicitly governed by the boundary conditions. Lower K_s values facilitate earlier biomass establishment at boundaries, reaching 27 kg/m^3 for $K_s = 10^6$ s compared to less than 3 kg/m^3 for $K_s = 10^8$ s. The temporal alignment between biomass peaks and free-water MC^* peaks (as shown in Figure 7a) confirms that:

- Boundary-driven moisture influx (associated with colonizing biomass) is the primary driver of free-water accumulation during early to mid-decay stages;
- This boundary-transport coupling means that K_s also controls moisture redistribution: faster boundary establishment enables more moisture influx sooner, which then diffuses inward.

5.4. Effect of Permeability Scaling (κ) on Moisture Redistribution

The permeability exponent κ determines the evolution of wood permeability in response to decay-induced structural modification (Equation (20)), where density loss from cell-wall degradation increases hydraulic conductivity. Adjusting κ within the tested range (5–25) resulted in a pronounced, nonlinear effect on free-water MC^* . Figure 8a demonstrates that low κ values cause persistent moisture accumulation, as permeability increases too slowly to remove boundary-supplied water. With increasing κ , free-water content declines progressively, indicating more efficient drainage and redistribution within the decaying wood matrix. At higher κ values, permeability enhancement occurs rapidly enough to prevent local water accumulation, leading to substantially lower MC^* levels by the end of the decay period.

This increased sensitivity arises because permeability influences moisture transport through coupled effects in the Darcy flux (Equation (19)), simultaneously accelerating water removal and smoothing internal moisture gradients. These results highlight the need of accurately characterizing decay–permeability relationships for the reliable prediction of moisture dynamics in decaying wood.

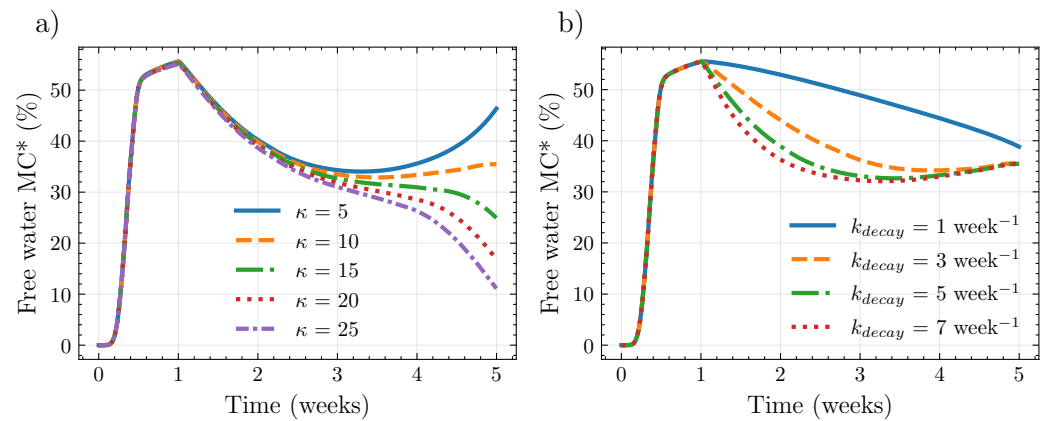


Figure 8. Effect of (a) permeability scaling parameter κ (values from 5 to 25) and (b) decay rate constant k_{decay} (values from 0.6×10^{-6} to $4.2 \times 10^{-6} \text{ s}^{-1}$) on free-water MC* evolution over the 35-day decay period.

Figure 8b illustrates the influence of the decay rate constant k_{decay} , which appears in the environmental decline function regulating both fungal activity and free-water removal. Varying k_{decay} over the tested range has little impact on the initial rise or timing of the free-water peak, with all curves converging during the first two weeks. In contrast, higher values accelerate the post-peak decline in free-water MC*. This trend indicates that early-stage free-water accumulation is governed primarily by boundary-driven moisture influx, whereas later-stage dynamics are dominated by removal and redistribution processes. The environmental decline term enforces a progressive reduction in free-water MC* at advanced decay stages, even in the presence of active fungal biomass. This behavior is consistent with experimental observations showing decreasing MC* with increasing mass loss.

5.5. Effect of Boundary Saturation Biomass Concentration (C_{biosat})

The saturation biomass concentration c_{biosat} defines the maximum fungal biomass that can be sustained at the wood–agar boundary, thereby establishing an upper limit on boundary-driven water influx. This parameter serves as a boundary saturation constraint, regulating the amount of colonizing biomass and associated water transport that can be supported at the interface where moisture enters the system. Figure 9 illustrates the influence of c_{biosat} on both biomass accumulation and free-water dynamics across a literature-informed range [56].

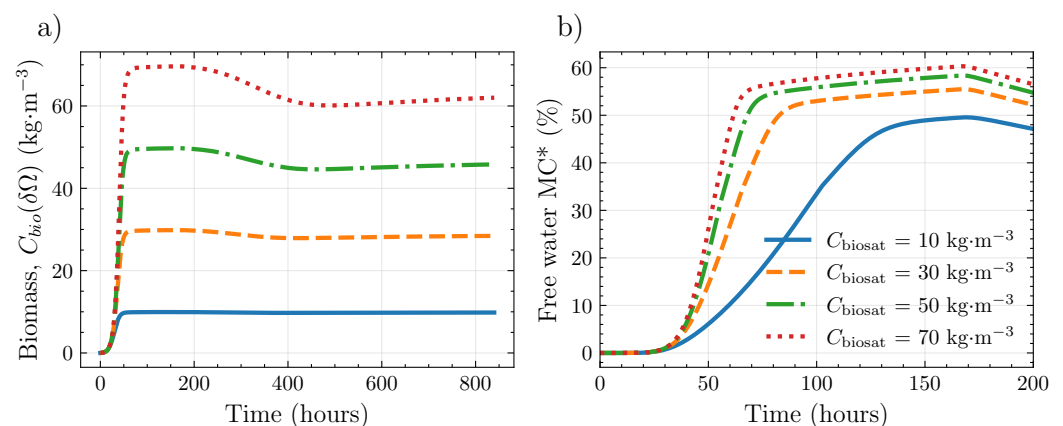


Figure 9. Effect of maximum biomass concentration c_{biosat} (values from 10 to 70 kg/m³) on (a) fungal biomass accumulation and (b) free-water MC* over the 35-day decay period.

Figure 9a demonstrates that increasing c_{biosat} consistently raises the final boundary biomass level, which occurs at approximately 50 to 60 h, while the overall growth dynamics remain largely unchanged. All scenarios display similar sigmoidal growth patterns, characterized by rapid establishment followed by a plateau, with peak biomass occurring at comparable times regardless of the saturation value. These results indicate that c_{biosat} determines the attainable boundary biomass limit, whereas the rate of colonization is governed by kinetic parameters. This observation aligns with its function as a boundary saturation limit in Equation (12): the flux term $-\mu(t)L_p(c_{\text{biosat}} - c_{\text{bio}})$ represents biomass influx from the agar substrate, which diminishes as the boundary concentration approaches c_{biosat} , independent of the colonization rate (controlled by μ_{max} and K_s).

Figure 9b reveals a direct and approximately proportional relationship between boundary biomass capacity and free-water accumulation. Higher c_{biosat} values permit greater boundary biomass establishment, which subsequently supports increased cumulative water influx. Although the magnitude of free-water accumulation scales with c_{biosat} , the timing of moisture peaks remains consistent across cases. This finding suggests that boundary biomass capacity primarily influences the magnitude of water influx, whereas the temporal onset is governed by colonization kinetics, which determine when boundary activity reaches its maximum.

5.6. Effect of Biomass Diffusivity (D_{bio})

The biomass diffusivity D_{bio} governs the spatial redistribution of fungal biomass within the wood matrix via Fickian diffusion (Equation (7)), which represents hyphal growth and translocation. Figure 10 illustrates the sensitivity of interior biomass concentration to D_{bio} over five orders of magnitude (10^{-13} to 10^{-9} m²/s), revealing its critical role in determining colonization patterns during the 5-week decay period.

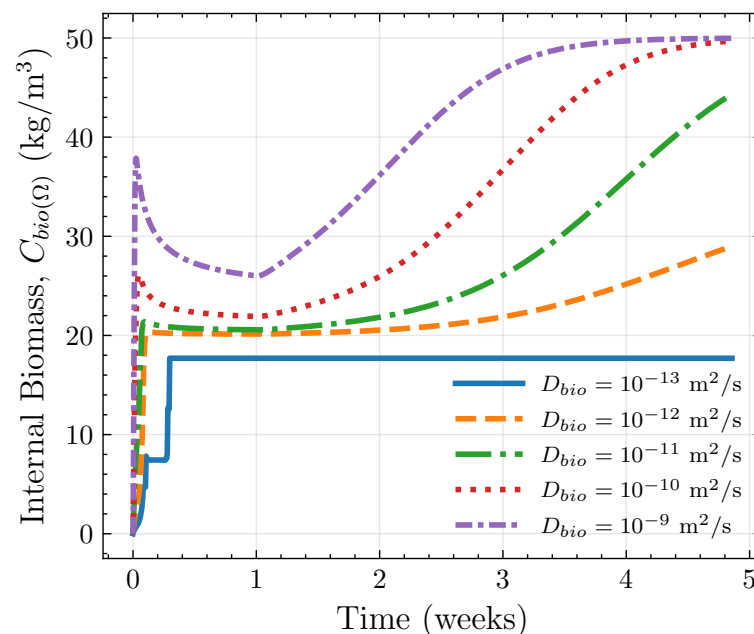


Figure 10. Effect of biomass diffusivity D_{bio} (values from 10^{-13} to 10^{-9} m²/s) on fungal biomass accumulation in the wood interior over the 35-day decay period.

Figure 10 shows the nonlinear sensitivity of interior biomass concentration to D_{bio} . At low diffusivity (10^{-13} m² s⁻¹), peak interior biomass is limited to approximately 18 kg m⁻³, indicating that fungal growth is confined near the boundary. Conversely, at high diffusivity (10^{-9} m² s⁻¹), interior biomass exceeds 35 kg m⁻³. Intermediate diffusivity values result in progressively higher interior concentrations, reflecting enhanced penetration and redistribution

of biomass within the wood. Although the magnitude of accumulation varies, all cases display similar temporal dynamics during the initial days, characterized by rapid biomass increase. These results suggest that D_{bio} primarily determines the spatial extent of colonization, while the timing is governed by growth kinetics. At low diffusivities (10^{-13} – 10^{-12} $\text{m}^2 \text{s}^{-1}$), steep spatial gradients persist and colonization remains localized near the surface. As diffusivity increases, biomass distribution becomes more uniform, and interior concentrations more closely follow boundary dynamics with reduced spatial lag.

5.7. Monte Carlo Uncertainty Quantification and Calibration

5.7.1. Model Predictions and Experimental Validation

Figure 11 presents the ensemble Monte Carlo predictions for free-water MC*, bound-water MC*, total MC*, and fungal biomass concentration over the five-week decay period, together with experimental LF-NMR measurements. Figure 11a demonstrates that the model captures the experimentally observed free-water dynamics. The ensemble mean (solid line) reflects the characteristic evolution: a rapid increase during the first week as boundary-driven water influx dominates, a peak in free-water content around 50 to 70% at weeks 1 to 2, and a gradual decline through weeks 3 to 5 as decay progresses and water-removal mechanisms become dominant. The 95% confidence interval (shaded region) contains the majority of experimental data points, indicating that the model uncertainty bounds appropriately represent the biological variability observed in the experiments. The interpretation of the early free-water peak as colonization-driven influx is supported by the experimental evidence: control samples placed on agar without fungal inoculation did not show free-water accumulation [30], ruling out agar vapor condensation as an alternative mechanism. However, while the Monte Carlo sensitivity structure at weeks 1–2—where boundary biomass capacity (c_{biosat}) and colonization rate (μ_{max}) are the dominant correlates of free-water MC*—is consistent with a boundary-driven mechanism, this evidence does not uniquely identify the underlying process. Alternative explanations that are not represented in the current model cannot be excluded. Colonization-driven moisture influx is therefore considered the most plausible interpretation given the available data, but dedicated experimental investigation of early-stage moisture dynamics during colonization (e.g., spatially resolved moisture tracking) would be needed to confirm or refine this interpretation.

Figure 11b presents bound-water predictions with substantially narrower confidence intervals compared to free water. The observed increase in mean bound-water MC* from approximately 30% to 35 to 40% results from the influence of the boost parameter α on bound-water MC*. Experimental data points are closely aligned with the model predictions, supporting the validity of the decay-modulated sorption isotherm formulation. The high correlation between α and bound-water MC* (0.9995) demonstrates that α effectively governs bound-water dynamics in the model. As shown in Section 5, this near-perfect correlation is a structural consequence of the equation system: the bound-water equilibrium target c_b^{eq} is functionally independent of all biological and transport parameters, depending only on α and the prescribed mass-loss trajectory. The seven remaining Monte Carlo parameters enter the biomass and free-water subsystems exclusively, and their influence on bound water through the indirect coupling path (via relative humidity) is negligible at the near-saturation conditions of this experiment. Consequently, the 0.9995 correlation quantitatively confirms that bound water during decay is governed by sorption thermodynamics rather than by transport or fungal kinetics—an informative physical finding, not an artifact of parameter fitting. Nevertheless, α remains a phenomenological parameter: it encodes the net macroscopic effect of competing processes (cell-wall degradation creating new sorption sites versus structural collapse reducing accessible volume) without resolving their individual contributions. The consistent bound-water MC* observed during decay is an experimental result reproduced across replicate tests [30].

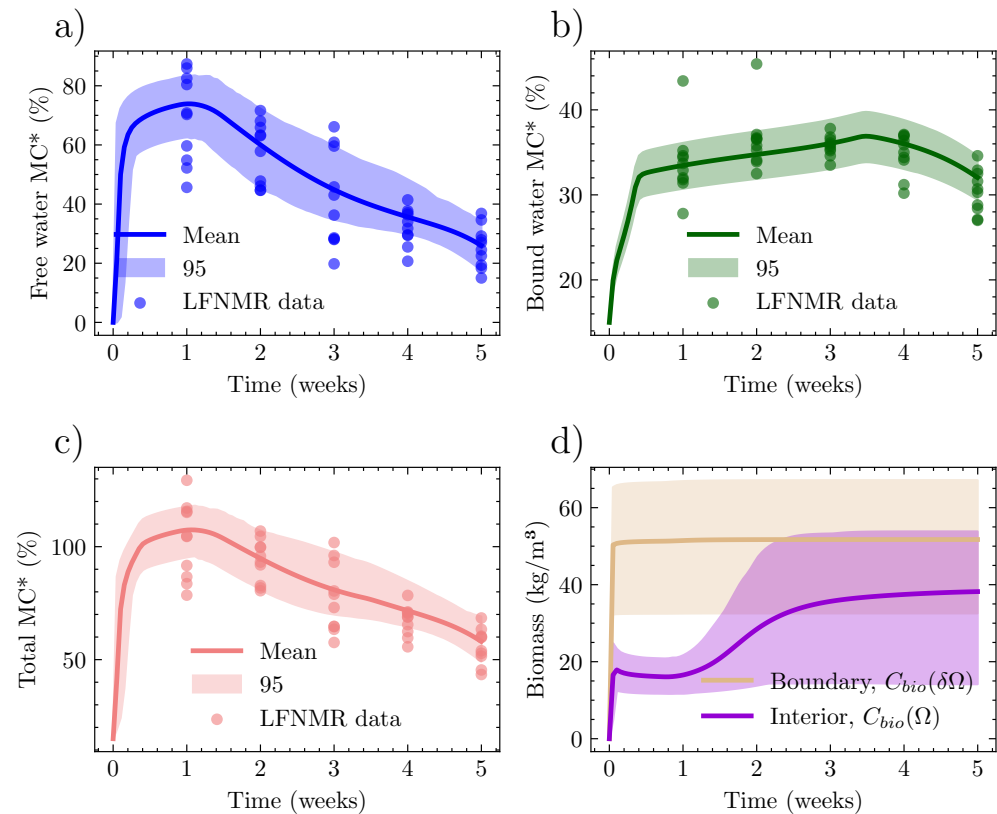


Figure 11. Monte Carlo ensemble predictions with experimental validation: (a) free-water MC*; (b) bound-water MC*; (c) total MC* combining free- and bound-water phases; (d) fungal biomass evolution at the colonizing surface and interior location. Shaded regions represent 95% confidence intervals from 300 Monte Carlo realizations, solid lines show ensemble means, and scatter points are individual experimental measurements from LF-NMR.

Figure 11c displays total MC* (free plus bound water), which evolves over time primarily due to changes in the free-water component, consistent with experimental observations. Figure 11d depicts the predicted fungal biomass evolution at two locations: the colonizing surface ($\delta\Omega$) and the interior volume (Ω). Although biomass is not measured experimentally, these predictions provide mechanistic insight into model behavior. Surface biomass establishes rapidly, reaching 45 to 55 kg/m³ by week 1 and plateauing near the boundary saturation limit C_{biosat} throughout the decay period. In contrast, interior biomass colonization is delayed due to the combined effects of diffusive transport (governed by D_{bio}) and local logistic growth following hyphal penetration. Figure 12 presents representative three-dimensional finite element fields to contextualize these spatial dynamics. The snapshots illustrate boundary-driven inward biomass penetration and the associated redistribution of free water over days 1, 4, and 8.

Table 3 provides a comparison between the LF-NMR experimental means and the Monte Carlo ensemble means for free water, bound water, and total moisture content at each weekly measurement interval. The model reproduces the experimental decline in free water from 68.99% (week 1) to 25.54% (week 5), with deviations ranging from +1.83% to +10.43%, indicating a slight overestimation during the early stages. Bound-water predictions remain within $\pm 5.5\%$ of the experimental measurements throughout the decay period, reflecting the near single-parameter control by α . Deviations in total moisture content remain below 7%.

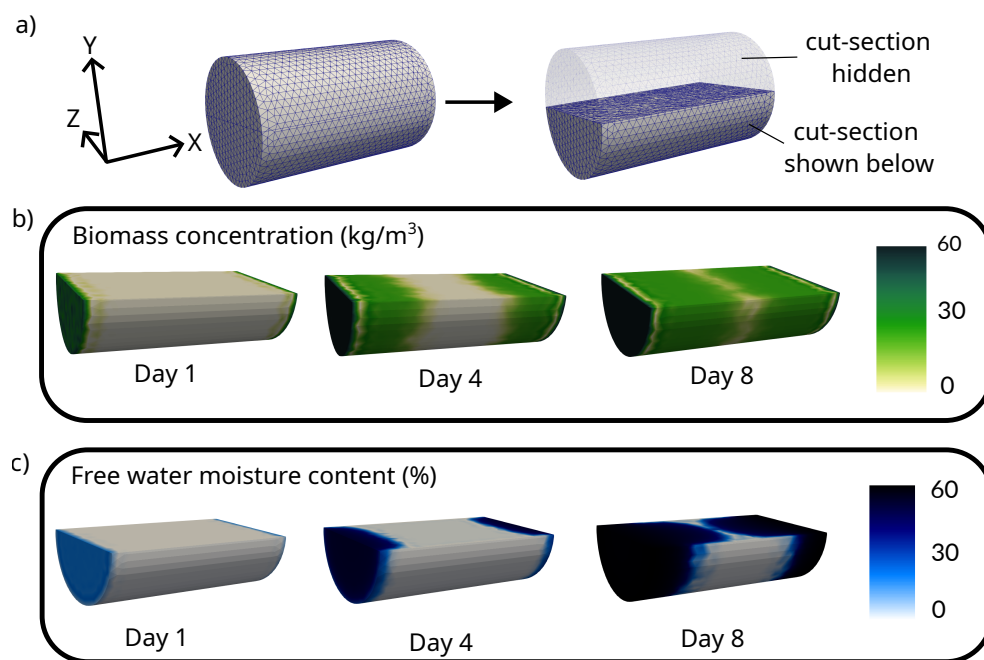


Figure 12. Representative 3D finite element simulation outputs used to visualize spatial gradients: (a) tetrahedral FE mesh of the wood sample and the cut-section view used for field visualization in (b,c); (b) fungal biomass concentration distribution at days 1, 4, and 8; (c) free-water moisture content distribution at days 1, 4, and 8.

Table 3. Comparison of weekly-averaged LF-NMR measurements and Monte Carlo ensemble means for free water, bound water, and total moisture content (MC*).

Week	Free Water (MC*)			Bound Water (MC*)			Total MC*		
	Expt.	Model	% Diff	Expt.	Model	% Diff	Expt.	Model	% Diff
1	68.99	73.89	+7.11	33.72	33.48	−0.72	102.71	107.37	+4.54
2	57.31	59.71	+4.20	36.39	34.77	−4.46	93.70	94.48	+0.84
3	41.64	45.13	+8.39	35.75	36.01	+0.73	77.39	81.14	+4.85
4	32.37	35.74	+10.43	34.82	36.04	+3.50	67.19	71.78	+6.84
5	25.54	26.00	+1.83	30.39	32.04	+5.44	55.93	58.05	+3.79

5.7.2. Time-Dependent Parameter Sensitivities

To quantify the evolution of parameter importance during the decay process, time-resolved Spearman correlation coefficients were computed between each varied parameter and the predicted outputs at weekly intervals (Figure 13). This analysis reveals shifts in model control from early colonization to late-stage moisture depletion.

(a) Free-water MC*

Figure 13a illustrates a distinct hierarchy of parameter influence on free-water MC*:

- Boundary biomass saturation (c_{biosat}): c_{biosat} remains the dominant parameter throughout the decay period, exhibiting strong positive correlations during weeks 1–4 ($\rho > 0.7$) and retaining influence in week 5 ($\rho \approx 0.54$). This pattern demonstrates its direct role in determining the maximum boundary-driven water influx capacity. The observed late-stage decline reflects reduced sensitivity as environmental constraints and removal processes become predominant.
- Colonization kinetics (μ_{max}, t_c): The maximum colonization rate μ_{max} shows moderate influence during early decay (week 1: $\rho \approx 0.6$), which diminishes steadily toward later stages. In contrast, the critical transition time t_c reaches peak influence during

mid-decay (weeks 2–4: $\rho \approx 0.4$). Collectively, these parameters regulate the timing and rate of early moisture accumulation.

- Environmental decline rate (k_{decay}): k_{decay} shifts from negligible influence during early colonization to a consistent negative correlation during weeks 2–5 ($\rho \approx -0.25$). This trend indicates that accelerated environmental decline suppresses sustained water delivery in later stages.
- Permeability evolution (κ): The permeability exponent displays a progressively stronger negative correlation, emerging as the dominant late-stage control by week 5 ($\rho \approx -0.72$). This outcome reflects the cumulative impact of decay-enhanced permeability on drainage and moisture removal, consistent with the exponential dependence $K \propto \rho^{-\kappa}$.
- Half-saturation constant (K_s): K_s exhibits a moderate negative correlation early in decay but rapidly loses influence, with correlation approaching zero by week 5. This pattern indicates diminishing substrate limitation after boundary colonization is established.

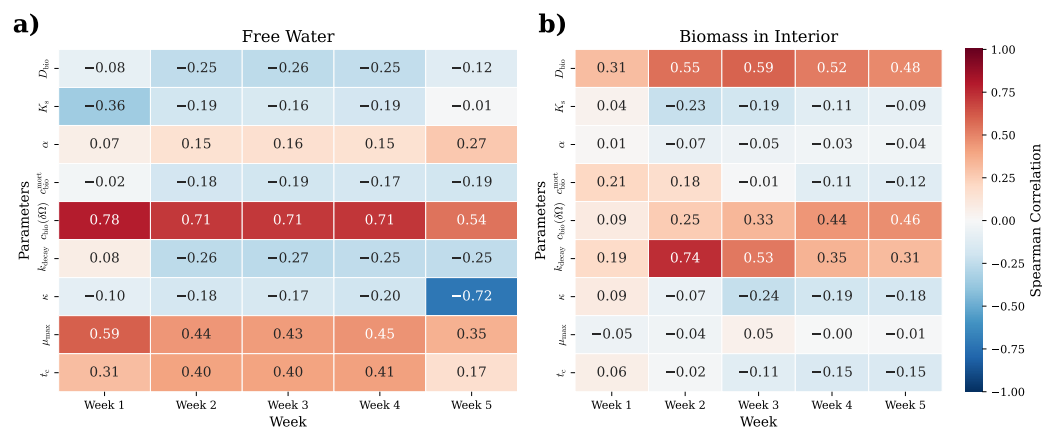


Figure 13. Time-dependent Spearman correlation heatmaps showing how parameter importance evolves across weeks 1–5 for: (a) free-water MC* and (b) interior biomass concentration. Color intensity indicates correlation strength (blue = negative, white = neutral, red = positive). Each cell shows the correlation coefficient between a parameter (rows) and the output variable at each weekly time point (columns).

(b) Interior biomass concentration

Figure 13b reveals a fundamentally different set of influential parameters for interior biomass concentration:

- Biomass diffusivity (D_{bio}): D_{bio} serves as the primary determinant of interior biomass concentration, with correlations increasing from early decay ($\rho \approx 0.3$) to a maximum during peak colonization ($\rho \approx 0.6$). These results confirm that interior colonization is diffusion-limited and governed by hyphal penetration rather than local growth rates.
- Boundary saturation (c_{biosat}): The influence of c_{biosat} on interior biomass increases steadily over time, reflecting the delayed transmission of boundary biomass capacity into the wood interior through diffusion.
- Decay rate (k_{decay}): k_{decay} exhibits a strong correlation during the mid-stage, indicating that environmental decline most strongly constrains interior biomass accumulation during active decay.
- Colonization rate (μ_{max}): μ_{max} shows negligible correlation with interior biomass concentration throughout, indicating that interior colonization is transport-limited rather than growth-limited within the explored parameter space.

Overall, the sensitivity analysis demonstrates a systematic shift in model control: early free-water dynamics are governed by boundary-driven influx (dominated by c_{biosat} and colonization kinetics), mid-stage behavior reflects increasing environmental suppression (k_{decay}), and late-stage moisture depletion is controlled by transport enhancement through evolving permeability (κ). In contrast, interior biomass accumulation is governed primarily by diffusive redistribution rather than growth kinetics.

5.7.3. Overall Parameter Importance Ranking

To complement the preceding time-resolved sensitivity analysis, the mean absolute Spearman correlation was calculated between each parameter and the three primary model outputs: free-water MC*, bound-water MC*, and interior biomass concentration, averaged across all weekly time points. This time-integrated metric quantifies the overall magnitude of each parameter's influence, regardless of sign, and offers a concise synthesis of parameter dominance throughout the 35-day decay period (Figure 14).

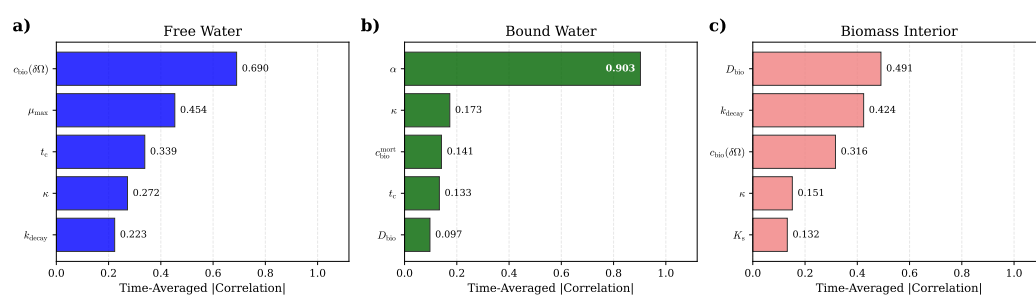


Figure 14. Overall parameter importance rankings based on time-averaged absolute Spearman correlations with model outputs from 300 Monte Carlo simulations: (a) free-water MC*, (b) bound-water MC*, and (c) fungal biomass. Bar heights represent mean absolute correlation magnitudes.

(a) Free-water MC*

Consistent with the temporal sensitivities described in Section 5.7.2, free-water MC* demonstrates moderate multi-parameter control. Boundary biomass saturation c_{biosat} is the primary contributor (mean $|\rho| = 0.69$), followed by colonization kinetics (μ_{max} , t_c) and permeability evolution (κ). This ranking indicates that free-water dynamics result from competition between boundary-driven influx capacity and removal processes governed by transport and decay, with no single parameter dominating across all stages.

(b) Bound-water MC*

In contrast to free water, bound-water MC* is governed by near single-parameter control. The boost factor α dominates the sensitivity ranking (mean $|\rho| = 0.90$), while all other parameters have minimal influence ($|\rho| < 0.2$). This result, which is not apparent in the time-resolved analysis, confirms that bound water is primarily determined by thermodynamic equilibrium between cell-wall sorption capacity and chemical potential, rather than by fungal growth or transport kinetics. This single-parameter dominance is a structural property of the PDE system: the bound-water equation (Equation (21)) has zero-flux boundary conditions, and its equilibrium target c_b^{eq} depends, at near-saturation, only on α and the externally prescribed density evolution, not on any of the biological or transport parameters varied in the Monte Carlo ensemble. The near-perfect correlation ($\rho = 0.9995$) therefore constitutes an informative finding—it quantitatively demonstrates that bound-water equilibrium during decay is thermodynamically controlled and structurally decoupled from fungal kinetics and moisture transport. Therefore, bound water can be calibrated independently using sorption isotherm measurements on degraded wood.

(c) Interior biomass concentration

The time-integrated ranking for biomass further supports the temporal findings: biomass predictions are strongly limited by capacity, with c_{biosat} dominating the sensitivity spectrum (mean $|\rho| = 0.97$), exceeding all other parameters by more than a factor of five. Growth rate parameters (μ_{max}) have a secondary influence by controlling the approach to saturation, while decay, diffusivity, and transport parameters contribute minimally to the final biomass level.

In summary, the time-resolved and time-integrated analyses reveal a clear hierarchical structure in model control. Free-water MC* requires multivariate calibration due to competing biological and transport mechanisms, whereas bound-water MC* and biomass concentration are governed by near single-parameter control, determined by α and c_{biosat} , respectively. This hierarchy informs experimental prioritization: boundary biomass capacity and sorption properties can be constrained independently, enabling calibration of the remaining free-water parameters using time-series moisture data.

5.7.4. Week-by-Week Variance Decomposition

To verify and consolidate the time-resolved and time-integrated sensitivity results, Pareto variance decomposition was performed for free-water MC*, bound-water MC*, and interior biomass at representative early (week 1), middle (week 3), and late (week 5) decay stages (Figure 15). This analysis quantifies the partitioning of total output variance among parameters at specific time points.

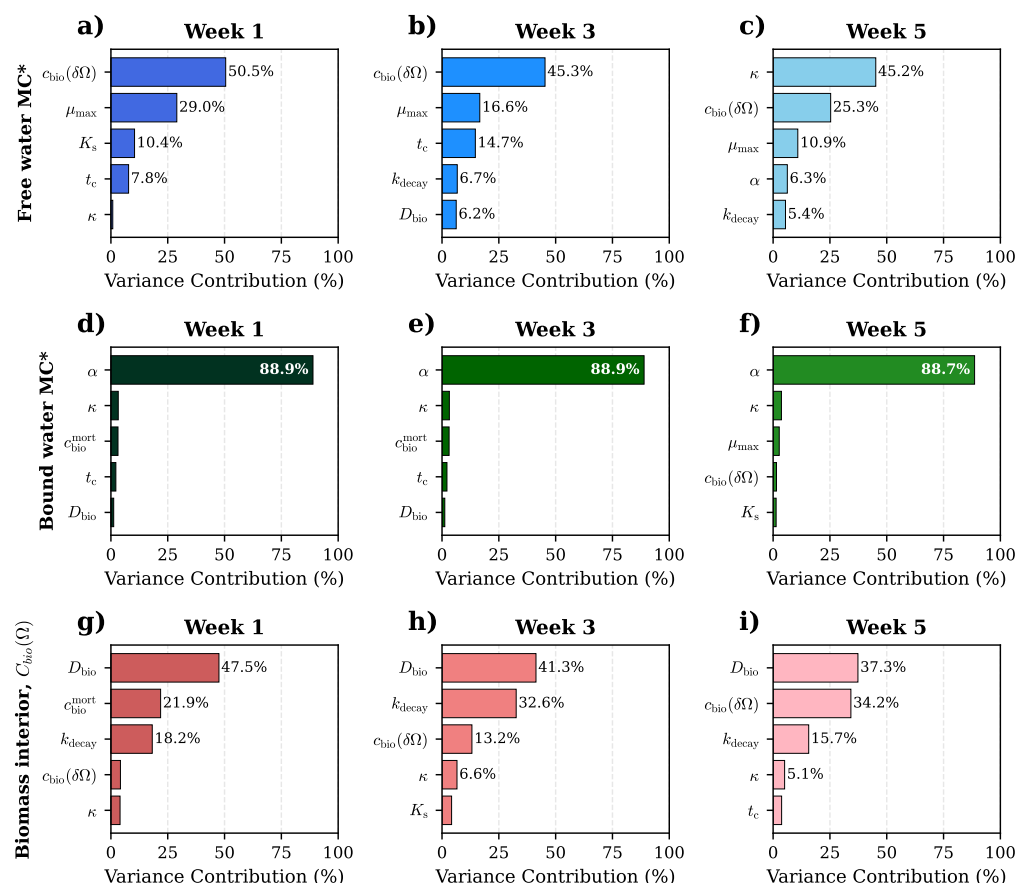


Figure 15. Week-by-week Pareto variance decomposition showing the percentage contribution of each parameter to total output variance. Top row (a–c): free-water MC* showing at weeks 1, 3 and 5. Middle row (d–f): bound-water MC* at weeks 1, 3 and 5. Bottom row (g–i): interior biomass variance showing at weeks 1, 3 and 5. Bars show individual variance contributions.

The variance decomposition for free-water MC* aligns with the time-dependent correlation analysis (Section 5.7.2). During early decay, free-water variance is dominated by boundary-driven parameters, with boundary biomass capacity and colonization kinetics explaining most of the variance at week 1 (Figure 15a). By week 3, variance contributions become more distributed, reflecting the mixed biological and physical control previously identified (Figure 15b). In late decay (week 5), variance is primarily attributed to the permeability exponent κ (Figure 15c), confirming the transition to transport-dominated moisture removal inferred from both the temporal sensitivities and the overall importance ranking (Section 5.7.3). For bound-water MC*, the variance decomposition is consistent with the overall importance ranking (Section 5.7.3); bound-water variance is fully controlled by α at all time points (Figure 15d–f). The negligible contribution of biological and transport parameters supports the conclusion that bound-water MC* is governed by equilibrium sorption behavior rather than fungal growth kinetics or transport processes. The evolution of interior biomass variance mirrors the transport-to-capacity transition identified in the correlation analysis (Section 5.7.2). Early variance is dominated by biomass diffusivity, indicating diffusion-limited penetration into the wood interior (Figure 15g). As decay progresses, the influence of the saturation limit increases (Figure 15h), and by week 5, diffusivity and boundary biomass capacity jointly dominate variance, confirming convergence toward a capacity-limited regime consistent with the overall ranking (Figure 15i).

5.8. Limitations of the Model

Although fungal biomass evolution is simulated through a reaction–diffusion equation with Monod-type growth kinetics, decay progression (mass loss) is not derived from biomass–substrate interaction but prescribed independently as an experimentally informed input. The model requires mass loss as a prescribed input rather than predicting it from first principles. Although mass loss governs permeability scaling and changes in sorption capacity, the model does not explicitly track the consumption of substrates such as cellulose, hemicellulose, and lignin by fungal metabolism. Implementing a substrate-based formulation with explicit degradation kinetics would address this limitation by computing mass loss from polymer depolymerization rates, thereby linking fungal growth directly to substrate availability instead of relying on time-based Monod kinetics. The current time-based Monod approach simplifies the underlying substrate-dependent growth dynamics. Fungal growth parameters (μ_{\max} , K_s , c_{biosat}) were estimated using Monte Carlo optimization rather than direct measurement due to the limited availability of experimental protocols for quantifying fungal biomass evolution in situ. Permeability evolution is modeled using empirical scaling that reflects the combined effects of pit membrane degradation, cell wall thinning, and void formation, but this approach does not distinguish individual contributions or predict the spatial heterogeneity of structural modifications. In brown-rot decay, permeability changes are anisotropic and primarily associated with pit membrane degradation and microcracking, rather than uniform scaling with density. Currently, no experimental permeability measurements during active decay are available to directly validate this formulation. Collectively, these limitations mean that the model's moisture transport predictions are conditioned on the specific experimentally observed decay trajectory and cannot be extrapolated to novel species, temperatures, or exposure conditions without new mass-loss data. The time-based growth formulation further restricts the transferability of the colonization dynamics to the tested experimental conditions.

The boost parameter (α) is used to phenomenologically correct near-saturation sorption behavior. If sorption isotherms were measured above the hygroscopic range at high relative humidities (95%–100%) on decayed wood samples, the actual equilibrium MC* could be directly incorporated into the model, potentially removing the need for this empirical

correction factor. While these phenomenological corrections reproduce observed behavior, they do not provide a mechanistic understanding of how decay alters cell wall chemistry and pore structure. Consequently, the model's bound-water predictions are empirically calibrated rather than derived from thermodynamic principles, and the value of α cannot be predicted *a priori* for untested decay stages, wood species, or environmental conditions. This constrains the model's claims regarding bound-water behavior to the calibration domain.

The model represents all moisture influx through boundary conditions proportional to colonizing biomass, which is appropriate for the experimental setup involving sterile wood placed on fungal colonized agar. However, this approach does not account for metabolic water generated internally via carbohydrate oxidation during fungal respiration. Although metabolic water production may be significant, it cannot be distinguished from boundary-transported water within the current framework. Separating metabolic water would require modeling it as a separate phase with its own conservation equation and source terms linked to substrate consumption rates, thereby increasing model complexity. This omission means that any moisture attributed to boundary transport may partially include metabolic contributions, which could affect the interpretation of the colonization-driven moisture influx mechanism. For the current experimental setup, where external moisture supply through agar contact is the dominant pathway, this effect is expected to be small, but it represents a source of uncertainty for more general applications.

Although anisotropic properties are applied to all physical parameters, including permeability, diffusivity, and thermal conductivity [27], the fungal parameters (μ_{\max} , K_s , D_{bio} , c_{biosat}) are treated as isotropic due to the limited availability of directional growth data. This simplification assumes that fungal colonization occurs equally in all directions, which may not be accurate for species that exhibit preferential longitudinal spread. The current model can accommodate anisotropic fungal parameters by adjusting the tensor components in the biomass diffusion term, provided that directional growth measurements are available to parameterize the anisotropy. Additionally, the boundary-driven formulation restricts generalization to field conditions with distributed moisture sources or cases where fungal colonization originates internally from wood containing dormant spores. Reformulation would be necessary to represent these scenarios, and the current results may serve as references for decay modeling in other wood-based composites. Consequently, the model's predictions of biomass-driven moisture transport are reliable only for configurations where colonization initiates exclusively from external surfaces, and the isotropic growth assumption may introduce directional errors in species with preferential longitudinal or radial hyphal spread.

6. Conclusions

A multi-phase bio-hygrothermal model was developed to integrate boundary-driven fungal biomass simulation with moisture transport analysis in wood during decay, and was validated using LF-NMR observations of *Coniophora puteana* colonization in Scots pine. This model integrates five governing equations for free water, bound water, vapor, biomass, and temperature fields, and incorporates boundary-driven fungal colonization, interior diffusion with logistic growth, Monod-type kinetics, and decay-induced changes in permeability and sorption behavior.

Monte Carlo uncertainty quantification, conducted with 300 parameter realizations, revealed temporal shifts in the dominant parameters controlling system behavior:

- Early moisture dynamics (weeks 1 to 2) are primarily influenced by boundary colonization capacity (c_{biosat} , 50% variance contribution) and growth rate (μ_{\max} , 29%), resulting in peak free-water MC* values of 50 to 70%.

- In late-stage moisture dynamics (week 5), permeability-driven drainage (κ , 45% variance) becomes dominant, accounting for the observed moisture decline despite ongoing decay.
- Bound-water MC^* remains quasi-deterministic, governed almost entirely by the boost parameter (α , 89% variance), which reflects thermodynamic equilibrium at sorption sites independent of fungal kinetics.

Parametric analysis indicated that permeability scaling yields the greatest variation (318%) in final MC^* among physical parameters, while μ_{\max} determines early colonization rates and associated water influx. The model reproduces the observed decrease in MC^* with advancing decay, consistent with the combined effects of boundary-driven water transport and permeability-enhanced drainage under the prescribed decay trajectory. Time-resolved correlation analysis identified a shift from colonization-dominated to transport-dominated control, highlighting implications for moisture-dependent wood durability under biological attack. The present framework constitutes a transport-response model for analyzing moisture behavior under externally defined decay progression: fungal biomass evolution is simulated, but mass loss is externally imposed rather than derived from biomass–substrate interaction, and bound-water equilibrium is governed by the phenomenological parameter α . Accordingly, the model does not represent a fully coupled bio-degradation system, and its conclusions are limited to the moisture-transport domain under known decay trajectories. Future research should incorporate substrate-coupled degradation kinetics and experimentally validated permeability evolution to extend the framework toward a fully predictive bio-hygrothermal model.

Author Contributions: R.D.D.: conceptualization, methodology, software, formal analysis, investigation, writing—original draft, writing—review and editing, visualization. T.B.: conceptualization, methodology, investigation, experimental work, funding acquisition, writing—review and editing. S.F.: funding acquisition, validation, resources, writing—review and editing, supervision, project administration. All authors have read and agreed to the published version of the manuscript.

Funding: This research was funded by project “Image-based Modelling of Water Transport In Wood including material biodegradation-WaterInWood”, Academy of Finland, Decision number 349194. The AI-TranspWood project, HORIZON-CL4-2023-RESILIENCE-01-23 (Grant Agreement 101138191), is also acknowledged. This project is co-funded by the European Union. Views and opinions expressed are however those of the author(s) only and do not necessarily reflect those of the European Union or HaDEA. Neither the European Union nor the granting authority can be held responsible for them.

Institutional Review Board Statement: Not applicable.

Informed Consent Statement: Not applicable.

Data Availability Statement: The data is available upon request from the corresponding author.

Conflicts of Interest: The authors declare no conflicts of interest.

Abbreviations

The following abbreviations are used in this manuscript:

LF-NMR	Low-Field Nuclear Magnetic Resonance
NMR	Nuclear Magnetic Resonance
MRI	Magnetic Resonance Imaging
FE	Finite Element
PDE	Partial Differential Equation
DOF	Degrees of Freedom

MC	Moisture Content
MC*	Mass Loss-Corrected Moisture Content
FSP	Fibre Saturation Point
RMSE	Root Mean Square Error
RH	Relative Humidity
EMC	Equilibrium Moisture Content
ML	Mass Loss
Nomenclature	
Concentrations	
c_i	Local concentration of species i (kg/m ³)
c_w	Free-water concentration (kg/m ³)
c_b	Bound-water concentration (kg/m ³)
c_v	Water-vapor concentration (kg/m ³)
c_{bio}	Fungal biomass concentration (kg/m ³)
c_{biosat}	Saturation limit of fungal biomass (kg/m ³)
$c_{v,\text{sat}}$	Saturation-vapor concentration (kg/m ³)
$c_{b,\text{eq}}$	Equilibrium bound-water concentration (kg/m ³)
Transport Properties	
D_{bio}	Effective mycelial diffusivity (m ² /s)
D_w	Free-water diffusion coefficient (m ² /s)
D_b	Bound-water diffusion coefficient (m ² /s)
D_v	Vapor diffusion coefficient (m ² /s)
K_w	Absolute permeability of wood (m ²)
K_r	Relative permeability (dimensionless)
Growth and Decay	
Parameters	
μ_{max}	Maximum boundary colonization rate (s ⁻¹)
K_s	Half-saturation constant for Monod kinetics (s)
k_{decay}	Environmental decline rate constant (s ⁻¹)
k_{mort}	Fungal mortality rate constant (s ⁻¹)
t_c	Critical time for decay onset (s)
α	Sorption isotherm scaling factor (dimensionless)
Fluxes and Source Terms	
\mathbf{J}_i	Flux vector of species i (kg/(m ² ·s))
\mathbf{J}_w	Free-water flux vector (kg/(m ² ·s))
\mathbf{J}_b	Bound-water flux vector (kg/(m ² ·s))
\mathbf{J}_v	Water-vapor flux vector (kg/(m ² ·s))
\mathbf{J}_{bio}	Hyphal biomass flux vector (kg/(m ² ·s))
\dot{S}_i	Net volumetric source/sink of phase i (kg/(m ³ ·s))
S_{growth}	Local fungal growth rate (kg/(m ³ ·s))
S_{mort}	Fungal mortality/decay rate (kg/(m ³ ·s))
$S_{w,\text{fungi}}$	Boundary water influx from fungal colonization (kg/(m ² ·s))
Material Properties	
$\rho_{\text{H}_2\text{O}}$	Density of water (kg/m ³)
μ_w	Dynamic viscosity of water (Pa·s)
ρ_d	Dry-wood density (kg/m ³)
ρ_d^{ini}	Initial dry-wood density (kg/m ³)
f_{lum}	Total lumen fraction (dimensionless)
$f_{\text{lum,gas}}$	Gas-filled lumen fraction (dimensionless)

Thermodynamic Properties

T	Temperature (K)
h	Specific enthalpy (J/kg)
h_v	Specific enthalpy of vapor (J/kg)
h_b	Specific enthalpy of bound water (J/kg)
h_w	Specific enthalpy of free water (J/kg)
P_g	Gaseous pressure (Pa)
P_c	Capillary pressure (Pa)
p_{atm}	Atmospheric pressure (Pa)
ϕ	Relative humidity (dimensionless)

Coupling Coefficients

H_{wb}	Coupling coefficient between free and bound water (s^{-1})
H_{bv}	Coupling coefficient between bound water and vapor (s^{-1})
H_{wv}	Coupling coefficient between free water and vapor (s^{-1})
\dot{c}_{wv}	Evaporation/condensation rate ($kg/(m^3 \cdot s)$)
\dot{c}_{wb}	Bound-to-free water transformation rate ($kg/(m^3 \cdot s)$)
\dot{c}_{bv}	Bound-to-vapor transformation rate ($kg/(m^3 \cdot s)$)

Boundary and Geometric

Parameter

k_{cw}	Free-water boundary transfer coefficient (m/s)
k_{cv}	Vapor boundary transfer coefficient (m/s)
L_p	Penetration depth characteristic length (m)
\mathbf{n}	Outward unit normal vector (dimensionless)
Ω	Computational domain
$\delta\Omega$	Boundary of computational domain

References

- Hyde, S.M.; Wood, P.M. A mechanism for production of hydroxyl radicals by the brown-rot fungus *Coniophora puteana*: Fe (III) reduction by cellobiose dehydrogenase and Fe (II) oxidation at a distance from the hyphae. *Microbiology* **1997**, *143*, 259–266. <https://doi.org/10.1099/00221287-143-1-259>.
- Irbe, I.; Andersons, B.; Chirkova, J.; Kallavus, U.; Andersone, I.; Faix, O. On the changes of pinewood (*Pinus sylvestris* L.) chemical composition and ultrastructure during the attack by brown-rot fungi *Postia placenta* and *Coniophora puteana*. *Int. Biodeterior. Biodegrad.* **2006**, *57*, 99–106. <https://doi.org/10.1016/j.ibiod.2005.12.002>.
- Novaes, E.; Kirst, M.; Chiang, V.; Winter-Sederoff, H.; Sederoff, R. Lignin and biomass: A negative correlation for wood formation and lignin content in trees. *Plant Physiol.* **2010**, *154*, 555–561. <https://doi.org/10.1104/pp.110.161281>.
- Brischke, C.; Alfredsen, G. Wood-water relationships and their role for wood susceptibility to fungal decay. *Appl. Microbiol. Biotechnol.* **2020**, *104*, 3781–3795. <https://doi.org/10.1007/s00253-020-10479-1>.
- Siau, J.F. *Transport Processes in Wood*; Springer Science & Business Media: Berlin/Heidelberg, Germany, 2012; Volume 2. <https://doi.org/10.1007/978-3-642-69213-0>.
- Skaar, C. *Wood-Water Relations*; Springer Science & Business Media: Berlin/Heidelberg, Germany, 2012. <https://doi.org/10.1007/978-3-642-73683-4>.
- Hiltunen, S.; Mankinen, A.; Javed, M.A.; Ahola, S.; Venäläinen, M.; Telkki, V.V. Characterization of the decay process of Scots pine caused by *Coniophora puteana* using NMR and MRI. *Holzforschung* **2020**, *74*, 1021–1032. <https://doi.org/10.1515/hf-2019-0246>.
- Thybring, E.E. Water relations in untreated and modified wood under brown-rot and white-rot decay. *Int. Biodeterior. Biodegrad.* **2017**, *118*, 134–142. <https://doi.org/10.1016/j.ibiod.2017.01.034>.
- Meyer, L.; Brischke, C. Fungal decay at different moisture levels of selected European-grown wood species. *Int. Biodeterior. Biodegrad.* **2015**, *103*, 23–29. <https://doi.org/10.1016/j.ibiod.2015.04.009>.
- Stienen, T.; Schmidt, O.; Huckfeldt, T. Wood decay by indoor basidiomycetes at different moisture and temperature. *Holzforschung* **2014**, *68*, 9–15. <https://doi.org/10.1515/hf-2013-0065>.
- Thybring, E.E.; Kymäläinen, M.; Rautkari, L. Experimental techniques for characterising water in wood covering the range from dry to fully water-saturated. *Wood Sci. Technol.* **2018**, *52*, 297–329. <https://doi.org/10.1007/s00226-017-0977-7>.

12. Fredriksson, M.; Thygesen, L.G. The states of water in Norway spruce (*Picea abies* (L.) Karst.) studied by low-field nuclear magnetic resonance (LFNMR) relaxometry: assignment of free-water populations based on quantitative wood anatomy. *Holzforschung* **2017**, *71*, 77–90. <https://doi.org/10.1515/hf-2016-0044>.
13. Zhou, M.; Caré, S.; Courtier-Murias, D.; Faure, P.; Rodts, S.; Coussot, P. Magnetic resonance imaging evidences of the impact of water sorption on hardwood capillary imbibition dynamics. *Wood Sci. Technol.* **2018**, *52*, 929–955. <https://doi.org/10.1007/s00226-018-1017-y>.
14. Kekkonen, P.M.; Ylisassi, A.; Telkki, V.V. Absorption of water in thermally modified pine wood as studied by nuclear magnetic resonance. *J. Phys. Chem. C* **2014**, *118*, 2146–2153. <https://doi.org/10.1021/jp411199r>.
15. Muller, U.; Bammer, R.; Halmschlager, E.; Stollberger, R.; Wimmer, R. Detection of fungal wood decay using magnetic resonance imaging. *Holz als Roh und Werkst.* **2001**, *59*, 190–194. <https://doi.org/10.1007/s001070100202>.
16. Kölle, M.; Crivelente Horta, M.A.; Benz, J.P.; Pilgård, A. Comparative transcriptomics during brown rot decay in three fungi reveals strain-specific degradative strategies and responses to wood acetylation. *Front. Fungal Biol.* **2021**, *2*, 701579. <https://doi.org/10.3389/ffunb.2021.701579>.
17. Xu, H.; Di, Y.; Cappellazzi, J.; Morrell, J.J. Effect of brown rot degradation on mass loss and compressive strength of Chinese poplar (*Populus simonii*). *Maderas. Cienc. Tecnología* **2019**, *21*, 341–346. <https://doi.org/10.4067/S0718-221X2019005000306>.
18. Beck, G.; Thybring, E.E.; Thygesen, L.G.; Hill, C. Characterization of moisture in acetylated and propionylated radiata pine using low-field nuclear magnetic resonance (LFNMR) relaxometry. *Holzforschung* **2018**, *72*, 225–233. <https://doi.org/10.1515/hf-2017-0072>.
19. Arantes, V.; Goodell, B. Current understanding of brown-rot fungal biodegradation mechanisms: A review. *Deterior. Prot. Sustain. Biomater.* **2014**, *1158*, 3–21. <https://doi.org/10.1021/bk-2014-1158.ch001>.
20. Goodell, B.; Zhu, Y.; Kim, S.; Kafle, K.; Eastwood, D.; Daniel, G.; Jellison, J.; Yoshida, M.; Groom, L.; Pingali, S.V.; et al. Modification of the nanostructure of lignocellulose cell walls via a non-enzymatic lignocellulose deconstruction system in brown rot wood-decay fungi. *Biotechnol. Biofuels* **2017**, *10*, 179. <https://doi.org/10.1186/s13068-017-0865-2>.
21. Arantes, V.; Milagres, A.M.F. Degradation of cellulosic and hemicellulosic substrates using a chelator-mediated Fenton reaction. *J. Chem. Technol. Biotechnol. Int. Res. Process Environ. Clean Technol.* **2006**, *81*, 413–419.
22. Younsi, R.; Kocaefe, D.; Poncsak, S.; Kocaefe, Y. Transient multiphase model for the high-temperature thermal treatment of wood. *AIChE J.* **2006**, *52*, 2340–2349. <https://doi.org/10.1002/aic.10860>.
23. Konopka, D.; Kaliske, M. Transient multi-Fickian hygro-mechanical analysis of wood. *Comput. Struct.* **2018**, *197*, 12–27. <https://doi.org/10.1016/j.compstruc.2017.11.012>.
24. Fortino, S.; Genoese, A.; Nunes, L.; Palma, P. Numerical modelling of the hygro-thermal response of timber bridges during their service life: A monitoring case-study. *Constr. Build. Mater.* **2013**, *47*, 1225–1234. <https://doi.org/10.1016/j.conbuildmat.2013.06.009>.
25. Krabbenhoft, K.; Damkilde, L. A model for non-Fickian moisture transfer in wood. *Mater. Struct.* **2004**, *37*, 615–622. <https://doi.org/10.1007/BF02483291>.
26. Autengruber, M.; Lukacevic, M.; Füssl, J. Finite-element-based moisture transport model for wood including free water above the fiber saturation point. *Int. J. Heat Mass Transf.* **2020**, *161*, 120228. <https://doi.org/10.1016/j.ijheatmasstransfer.2020.120228>.
27. Dsouza, R.D.; Harjupatana, T.; Miettinen, A.; Brandstätter, F.; Harju, A.; Venäläinen, M.; Möttönen, V.; Borrega, M.; Paaianen, A.; Füssl, J.; et al. Multi-phase model for moisture transport in wood supported by X-ray computed tomography data. *Wood Sci. Technol.* **2025**, *59*, 31. <https://doi.org/10.1007/s00226-025-01635-9>.
28. Brischke, C.; Alfredsen, G.; Humar, M.; Conti, E.; Cookson, L.; Emmerich, L.; Flæte, P.O.; Fortino, S.; Francis, L.; Hundhausen, U.; et al. Modelling the Material Resistance of Wood—Part 2: Validation and Optimization of the Meyer–Veltrup Model. *Forests* **2021**, *12*, 576. <https://doi.org/10.3390/f12050576>.
29. Marais, B.N.; van Niekerk, P.B.; Brischke, C. Studies into Fungal Decay of Wood in Ground Contact—Part 2: Development of a Dose–Response Model to Predict Decay Rate. *Forests* **2021**, *12*, 698. <https://doi.org/10.3390/f12060698>.
30. Belt, T.; Treu, A.; Möttönen, V.; Altgen, M. Moisture dynamics during *Coniophora puteana* brown rot degradation of Scots pine sapwood. *Int. Biodeterior. Biodegrad.* **2026**, *209*, 106296.
31. Brandstätter, F. Numerical Prediction of Moisture Distributions Below and Above the Fiber Saturation Point and Their Impact on Crack Behavior in Timber Elements. Ph.D. Thesis, Technische Universität Wien, Wien, Austria, 2025. <https://doi.org/10.34726/hss.2025.130001>.
32. Carr, H.Y.; Purcell, E.M. Effects of diffusion on free precession in nuclear magnetic resonance experiments. *Phys. Rev.* **1954**, *94*, 630. <https://doi.org/10.1103/PhysRev.94.630>.
33. Meiboom, S.; Gill, D. Modified spin-echo method for measuring nuclear relaxation times. *Rev. Sci. Instrum.* **1958**, *29*, 688–691. <https://doi.org/10.1063/1.1716296>.
34. Lawson, C.L.; Hanson, R.J. Linear least squares with linear inequality constraints. In *Solving Least Squares Problems*; Society for Industrial and Applied Mathematics: Philadelphia, PA, USA, 1974; pp. 158–173. <https://doi.org/10.1137/1.9781611971217.ch23>.

35. Whittall, K.P.; Bronskill, M.J.; Henkelman, R.M. Investigation of analysis techniques for complicated NMR relaxation data. *J. Magn. Reson.* (1969) **1991**, *95*, 221–234. [https://doi.org/10.1016/0022-2364\(91\)90213-D](https://doi.org/10.1016/0022-2364(91)90213-D).
36. Araujo, C.; MacKay, A.; Hailey, J.; Whittall, K.; Le, H. Proton magnetic resonance techniques for characterization of water in wood: application to white spruce. *Wood Sci. Technol.* **1992**, *26*, 101–113.
37. Jokisaari, J. Moisture in softwoods: fiber saturation point, hydroxyl site content, and the amount of micropores as determined from NMR relaxation time distributions. *Holzforschung* **2013**, *67*, 291–300.
38. Beck, G. Leachability and decay resistance of wood polyesterified with sorbitol and citric acid. *Forests* **2020**, *11*, 650.
39. Lee, K.H.; Wi, S.G.; Singh, A.P.; Kim, Y.S. Micromorphological characteristics of decayed wood and laccase produced by the brown-rot fungus *Coniophora puteana*. *J. Wood Sci.* **2004**, *50*, 281–284. <https://doi.org/10.1007/s10086-003-0558-2>.
40. Kleist, G.; Schmitt, U. Characterisation of a soft rot-like decay pattern caused by *Coniophora puteana* (Schum.) Karst. in Sapelli wood (*Entandrophragma cylindricum* Sprague). *Holzforschung* **2001**, *55*, 437–442. <https://doi.org/10.1515/HF.2001.093>.
41. Du, H.; Ayouz, M.; Lv, P.; Perré, P. A lattice-based system for modeling fungal mycelial growth in complex environments. *Phys. A Stat. Mech. Its Appl.* **2018**, *511*, 191–206. <https://doi.org/10.1016/j.physa.2018.07.051>.
42. Davidson, F.; Park, A. A mathematical model for fungal development in heterogeneous environments. *Appl. Math. Lett.* **1998**, *11*, 51–56.
43. Ogawa, K.; Yashima, T. Enhanced water uptake in the longitudinal direction by shiitake mycelium in shiitake cultivation logs: Increase in effective diffusion coefficient based on mass of liquid water uptake. *Wood Sci. Technol.* **2021**, *55*, 1237–1267. <https://doi.org/10.1007/s00226-021-01313-6>.
44. Monod, J. The growth of bacterial cultures. *Sel. Pap. Mol. Biol. Jacques Monod* **2012**, *139*, 606.
45. Wang, Y.; Feng, Y.; Xu, X.; Jin, S. Local Fractional Modeling of Microorganism Physiology Arising in Wastewater Treatment: Lawrence–McCarty Model in Cantor Sets. *Fractal Fract.* **2025**, *9*, 413. <https://doi.org/10.3390/fractalfract9070413>.
46. Liu, Y. Overview of some theoretical approaches for derivation of the Monod equation. *Appl. Microbiol. Biotechnol.* **2007**, *73*, 1241–1250. <https://doi.org/10.1007/s00253-006-0717-7>.
47. Freschet, G.T.; Weedon, J.T.; Aerts, R.; van Hal, J.R.; Cornelissen, J.H. Interspecific differences in wood decay rates: Insights from a new short-term method to study long-term wood decomposition. *J. Ecol.* **2012**, *100*, 161–170. <https://doi.org/10.1111/j.1365-2745.2011.01896.x>.
48. Touloukian, Y.; Saxena, S.; Hestermans, P. *Thermophysical Properties of Matter—the TPRC Data Series. Volume 11. Viscosity*; Defense Technical Information Center: Fort Belvoir, VA, USA, 1975.
49. Frandsen, H.L. Selected Constitutive Models for Simulating the Hygromechanical Response of Wood. Ph.D. Thesis, Aalborg University, Aalborg, Denmark, 2007.
50. Hailwood, A.; Horrobin, S. Absorption of water by polymers: Analysis in terms of a simple model. *Trans. Faraday Soc.* **1946**, *42*, B084–B092.
51. Baratta, I.A.; Dean, J.P.; Dokken, J.S.; Habera, M.; Hale, J.S.; Richardson, C.N.; Rognes, M.E.; Scroggs, M.W.; Sime, N.; Wells, G.N. DOLFINx: The next generation FEniCS problem solving environment. *Zenodo* **2023**. <https://doi.org/10.5281/zenodo.10447666>.
52. Scroggs, M.W.; Baratta, I.A.; Richardson, C.N.; Wells, G.N. Basix: A runtime finite element basis evaluation library. *J. Open Source Softw.* **2022**, *7*, 3982. <https://doi.org/10.21105/joss.03982>.
53. Alnaes, M.S.; Logg, A.; Ølgaard, K.B.; Rognes, M.E.; Wells, G.N. Unified Form Language: A domain-specific language for weak formulations of partial differential equations. *ACM Trans. Math. Softw.* **2014**, *40*, 9. <https://doi.org/10.1145/2566630>.
54. Geuzaine, C.; Remacle, J.F. Gmsh: A three-dimensional finite element mesh generator with built-in pre- and post-processing facilities. *Int. J. Numer. Methods Eng.* **2009**, *79*, 1309–1331.
55. Nasr, A.; Niklewski, J.; Björnsson, I.; Johansson, J. Probabilistic analysis of climate change impact on fungal decay of timber elements in ground contact and their long-term structural performance. *Wood Mater. Sci. Eng.* **2023**, *18*, 594–606. <https://doi.org/10.1080/17480272.2022.2057813>.
56. Nussbaumer, M.; Karl, T.; Benz, J.P. Quantification of fungal biomass in mycelium composites made from diverse biogenic side streams. *Fungal Biol. Biotechnol.* **2024**, *11*, 20. <https://doi.org/10.1186/s40694-024-00189-y>.
57. Boswell, G.P.; Jacobs, H.; Ritz, K.; Gadd, G.M.; Davidson, F.A. The development of fungal networks in complex environments. *Bull. Math. Biol.* **2007**, *69*, 605–634. <https://doi.org/10.1007/s11538-005-9056-6>.
58. Du, H.; Lv, P.; Ayouz, M.; Besserer, A.; Perré, P. Morphological characterization and quantification of the mycelial growth of the brown-rot fungus *postia placenta* for modeling purposes. *PLoS ONE* **2016**, *11*, e0162469. <https://doi.org/10.1371/journal.pone.0162469>.

Disclaimer/Publisher’s Note: The statements, opinions and data contained in all publications are solely those of the individual author(s) and contributor(s) and not of MDPI and/or the editor(s). MDPI and/or the editor(s) disclaim responsibility for any injury to people or property resulting from any ideas, methods, instructions or products referred to in the content.